

Design of electrical transmission lines for the measurements in a rubidium vapor cell

Bachelor Thesis

Kateryna Guguieva

Supervisors:

María Félix Rosa

(Institute of Electrical and Optical Communications Engineering)

Johannes Schmidt

*(Institute for Large Area Microelectronics,
5th Institute of Physics)*

November 2016

Contents

Contents	1
Symbols and abbreviations	2
Zusammenfassung	4
Abstract	5
Assignment	6
1 Introduction	7
2 Transmission line theory	8
2.1 Transmission line model	8
2.2 Attenuation mechanisms	13
2.2.1 Attenuation due to metal conductivity	14
2.2.2 Attenuation due to the dielectric loss	15
2.3 Scattering matrix	18
2.4 Coplanar waveguide.....	20
3 Atomic vapor cell	24
3.1 Fundamentals of the rubidium vapor cell	24
3.2 Glass-to-glass anodic bonding	28
4 Design and simulation of transmission lines	30
5 Fabrication	34
6 Measurement results	37
6.1 Overview over the measurement results	37
6.2 Analysis of simulations and measurements	41
6.3 Final structure of the coplanar waveguide	47
7 Summary and outlook	48
Appendix	49
Simulation in CST® MWS®	49
Bibliography	52
Acknowledgement	54
Erklärung	55

Symbols and abbreviations

List of symbols

Notation	Description	Units
A	(Cross-sectional) area	m ²
C	Capacitance	F
C'	Capacitance per unit length	F/m
D	Electric displacement field	As/m ²
E	Electric field strength	V/m
f	Frequency	Hz
G	Conductance	S
G'	Conductance per unit length	S/m
I	Current	A
J	Current density	A/m ²
L	Inductance	L
L'	Inductance per unit length	L/m
n	Refractive index of the material	
P	Polarisation density	As/m ²
R	Resistance	Ω
R'	Resistance per unit length	Ω/m
R _s	Sheet resistance	Ω/□
V	Voltage	V
Z ₀	Characteristic impedance of the transmission line	Ω
α	Attenuation constant	1/m
α _c	Attenuation due to metal conductivity	1/m
α _d	Dissipation factor	1/m
β	Phase constant	1/m
γ	Propagation constant	1/m
σ	Electrical specific conductivity	S/m
δ _s	Skin depth	m
ε	Electromagnetic force	V
ε	Absolute permittivity of the medium	F/m
ε _r	Relative permittivity	
λ ₀	Wavelength in vacuum	m
λ _l	Wavelength of the transmission line	m
μ	Absolute permeability of the medium	F/m
μ _r	Relative permeability	
v _p	Phase velocity	m/s
Φ	Magnetic flux	W
φ	Phase angle	
χ _e	Electric susceptibility	
ω	Angular frequency	1/s

Physical constants

Notation	Description	Value
c	Speed of light	2.99×10^8 m/s
ϵ_0	Dielectric constant	8.854×10^{-12} F/m
μ_0	Permeability constant	$4\pi \times 10^{-7}$ H/m

Abbreviations

AC	Alternating current
Al	Aluminum
CPW	Coplanar waveguide
Cr	Chromium
DC	Direct current
EIT	Electromagnetically induced transparency
MoTa	Molybdenum-Tantalum
PECVD	Plasma enhanced chemical vapor deposition
Rb	Rubidium
RIE	Reactive ion etching
SiO ₂	Silicon dioxide
SiN	Silicon nitride

Zusammenfassung

Zurzeit werden viele Versuche mit Rydberg-Atomen am 5. Physikalischen Institut der Universität Stuttgart durchgeführt. Zu diesem Zweck wird am Institut mit Rubidium Dampfzellen gearbeitet. Einige der Experimente untersuchen Wechselwirkung zwischen den Rydberg-Atomen und dem elektrischen Feld. Bisher wurde das elektrische Feld außerhalb der Zelle z. B. mithilfe von Horn-Antennen angelegt. Es ist aber unmöglich in diesem Fall die Feldstärke in der Zelle selbst zu messen. Aus diesem Grund sollen integrierte Wellenleiter entworfen werden, die die Zelle durchqueren. Dabei soll Zellaufbau und folgendes Prozess des hermetischen Zellverschließens in Kauf genommen werden. Um diese Aufgabe zu realisieren, wurden koplanare Wellenleiter angesichts ihrer einfacheren Herstellung und besseren Ausführung als Streifenleitung gewählt. Zuerst wurden sie am Institut für Elektrische und Optische Nachrichtentechnik mithilfe von CST[®] MWS[®] für eine Frequenz von 100 MHz simuliert. Aufgrund der Zellenbreite von 4 cm, die die Wellenleiterlänge definiert, ist es nicht möglich, die ganze Struktur zu simulieren. Anstatt dessen wurden kürzere Abschnitte simuliert, um die charakteristische Impedanz und die Ausbreitungskonstante abzuschätzen. Das genügt vollkommen, weil die letzten unabhängig von der Wellenleiterlänge sind. Um Verluste zu analysieren, wurden die Wellenleiter in mehreren Längen entworfen. Die Wellenleiter wurden im Reinraum des Institutes für Großflächige Mikroelektronik der Universität Stuttgart hergestellt. Dazu wurden mehrere Substrate mit verschiedenen Metallen und mit verschiedenen Herstellungsverfahren realisiert. Die einzelnen Wellenleiter wurden nach der Messung verglichen. Eine große Rolle spielt hierbei die Dämpfung. Die Simulationsergebnisse wurden mit den Ergebnissen der Messung verglichen und zeigen eine gute Übereinstimmung. Die endgültige Struktur, ein Glassubstrat mit 4 cm langen Wellenleitern und gebondetem Glasrahmen, hat Verluste von etwa 4.6 dB bei der Frequenz von 100 MHz gezeigt.

Abstract

Experiments with Rydberg electromagnetically induced transparency (EIT) using atomic vapor cell are currently taking place in the 5th Institute of Physics. These experiments investigate the interaction between the Rydberg atoms and an electric field. They were successfully completed with an electric field created externally but in this case there is no possibility to measure the field strength inside the cell. Therefore integrated transmission lines crossing the cell have to be fabricated. The cell structure and the following cell sealing process should be taken into account during the design of the transmission lines. For this purpose the coplanar waveguides (CPW) are chosen. First they are simulated at the Institute of Electrical and Optical Communication Engineering of the University of Stuttgart using CST[®] MWS[®] at a frequency of 100 MHz. Considering the length of the coplanar waveguides defined by the cell width (4 cm), it is complicated to simulate the whole structure. Since the characteristic impedance is independent of length, shorter sections of 0.5 cm are designed and simulated. This provides information about the characteristic impedance and the propagation constant, but doesn't estimate real losses. To estimate losses the CPWs are designed with several lengths. The CPWs are fabricated in the clean room at the Institute of Large Area Microelectronics of the University of Stuttgart. Several wafers are structured applying various materials and fabrication techniques to find out the best way to maintain as good performance as possible, because for the given length even small losses matter. After fabrication, the CPWs are measured and applied fabrication methods compared and analysed. Moreover measurement results are compared with the simulation and showed good agreement. The final structure consisting of the substrate with structured CPWs and bonded glass frame on top of the CPWs is found to have 4.6 dB losses.

Assignment

This work deals with the design and fabrication of transmission lines which are integrated inside an atomic vapor cell. These transmission lines should provide an electric field at a frequency of 100 MHz, so that the interaction of electric field and rubidium atoms excited to the Rydberg state can be investigated. During the course of this work several problems have to be resolved. First the suitable structure has to be selected among available options regarding measurement and fabrication equipment. This important step is carefully performed by simulating the structure in order to predict its behavior. It should be taken into account that the fabrication methods and materials of the transmission lines are restricted by a cell geometry and the subsequent cell sealing method. Solving all these issues the assignment can be successfully accomplished.

1 Introduction

With the expanding developing of complicated electronic circuits and diminishing chip sizes more effective sensing methods have to be engineered. Currently atom-based measurement techniques in many areas are gaining a lot of attention. For this reason an atomic vapor cell was developed at the 5th Institute of Physics, which contains high vacuum for relatively long time and allows therefore experiments at room temperature without additional complexity. The cells are filled with alkali atoms. During experiments the atoms are excited to the Rydberg states; these are highly excited atoms with hydrogen like behavior. They have large radius and high polarizability which can be used for quantum computing research field. Moreover they are extremely sensitive to electric fields. It is beneficial for electric field sensing and can be applied e.g. for characterisation of small integrated circuits or metamaterials. In many cases it is difficult to use an antenna even geometrically, let alone that antenna itself is made of metal and severely perturbs an electric field of the device under test. Another huge advantage of atom-based measurements is the self-calibrating platform based on natural constants which can be easily calculated and don't change from sample to sample. One particular experiment which is performed at the 5th Institute of Physics is the optical transmission switching by applying an electric field. This phenomenon is called electromagnetically induced transparency (EIT) and will be discussed in the Chapter 3.1. The experiments were already done with the field created outside the cell using horn antenna or either coplanar waveguides placed under the cell. The fields were detected and imaged. Nevertheless this method doesn't allow the measuring of an electric field inside the cell which in some respects draws back the full overview of the results. To be able to create and measure an electric field inside the cell some integrated transmission lines have to be fabricated. This is the very purpose of this bachelor thesis.

After discussion of theoretical knowledge behind the working principle of the transmission lines presented in Chapter 2, the brief overview over the atomic vapor cell and Rydberg EIT is given in Chapter 3. There the cell structure and fabrication is discussed as it is an important information regarding the transmission line design. Additionally the Rydberg EIT is shortly described. Further the whole process from simulations to characterisation is presented. In the Chapter 4 the choice of transmission lines is reasoned and simulation approach at 100 MHz is to be found. The fabrication process in the clean room including the basic description of deposition and structuring techniques is given in the Chapter 5. Finally all the measurement results are in detail discussed in the Chapter 6 along with the characterisation. First the overview of the compared fabrication methods is presented with the outlook for future applications at higher frequencies. Besides the simulation results are compared with measurements. At last the characteristic of the wanted coplanar waveguide is given. In the Chapter 7 follows eventually the summary of this thesis and outlook for future research.

2 Transmission line theory

2.1 Transmission line model

By speaking about transmission lines the two- or multi-conductor structures that support transversal electromagnetic (TEM) or non-TEM propagating modes are often meant. The TEM transmission line can be characterised using the lumped-element circuit model [1, 2] with R' , G' , L' and C' as length dependent parameters. They are defined as follows:

- R' is a series resistance per unit length in Ω/m ,
- L' is a series inductance per unit length in H/m ,
- G' is a shunt conductance per unit length in S/m and
- C' is a shunt capacitance per unit length in F/m .

The model for a small section of transmission line is presented in Figure 2.1; the series setup of such sections can be viewed as a finite transmission line.

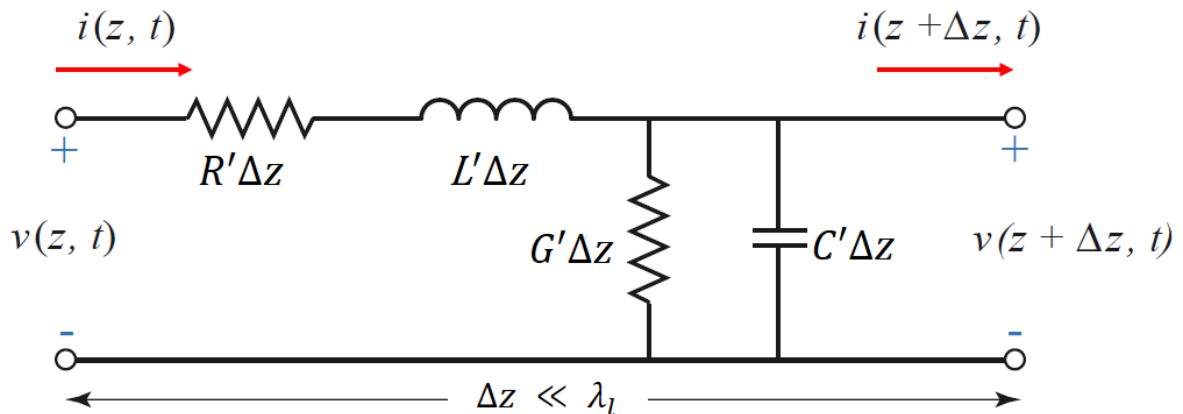


Figure 2.1: Lumped-element circuit model for an infinitesimal section of transmission line.

Source: [1]

This transmission line model is schematically represented by a pair of parallel conductors showing certain characteristics due to distributed capacitance and inductance along its length. The voltages between the conductors and the current in the conductors are considered as the state variables.

If an alternating voltage is applied between two conductors it creates an electric field between them; thus the shunt capacitance C would charge up. This gives rise to a charging current drawn from the source by the parallel wires, which is proportional to the rate of change of the voltage:

$$i = C \frac{du}{dt}. \quad (2.1)$$

This effect is referred to as a dielectric “leakage” G , as the charging current represents the leakage current between the signal wire and the return wire. However this charging current

will be limited by the self-inductance L of the conductors. The wires develop the magnetic fields as they carry the charging current for capacitance, and the energy stored in this magnetic field is proportional to the rate of change of the current:

$$u = L \frac{di}{dt}. \quad (2.2)$$

It leads to a voltage drop, which in their turn limits the charging current preventing it from reaching an infinite magnitude.

Kirchhoff's voltage law and Kirchhoff's current law can be applied to the circuit from Figure 2.1 to obtain

$$v(z, t) - R' \Delta z i(z, t) - L' \Delta z \frac{\partial i(z, t)}{\partial t} - v(z + \Delta z, t) = 0 \quad (2.3a)$$

and

$$i(z, t) - G' \Delta z v(z + \Delta z, t) - C' \Delta z \frac{\partial v(z + \Delta z, t)}{\partial t} - i(z + \Delta z, t) = 0 \quad (2.3b)$$

Respectively [1].

Dividing these equations by the infinitesimal length $\Delta z \rightarrow 0$ provides:

$$-R' i(z, t) - L' \frac{\partial i(z, t)}{\partial t} - \lim_{\Delta z \rightarrow 0} \frac{v(z + \Delta z, t)}{\Delta z} = 0, \quad (2.4a)$$

$$-G' v(z + \Delta z, t) - C' \frac{\partial v(z + \Delta z, t)}{\partial t} - \lim_{\Delta z \rightarrow 0} \frac{i(z + \Delta z, t)}{\Delta z} = 0. \quad (2.4b)$$

To evaluate voltage and current functions at a point $(z + \Delta z, t)$, a Taylor series expansion of the form

$$T_n(x, a) = \sum_{n=0}^{\infty} \frac{d^n f(x)}{dx^n} \Big|_{x=a} (x - a)^n \frac{1}{n!} \quad (2.5)$$

can be used, where a is the evaluation point. Thus, the approximation for $v(z + \Delta z, t)$ around the point z

$$v(z + \Delta z, t) = \sum_{n=0}^{\infty} \frac{d^n v(z, t)}{dz^n} \Big|_{z=\Delta z, t} (\Delta z, t)^n \frac{1}{n!} \quad (2.6)$$

can be calculated for the first two terms of the series to:

$$v(z + \Delta z, t) = v(z) + \frac{dv(z, t)}{dz} \Delta z. \quad (2.7a)$$

In the analogous way the approximation for the current is obtained:

$$i(z + \Delta z, t) = i(z) + \frac{di(z, t)}{dz} \Delta z. \quad (2.7b)$$

Placing (2.7a) in (2.4a) and (2.7b) in (2.4b) yields the following first-order partial differential equations:

$$\frac{\partial v(z, t)}{\partial z} = -R' i(z, t) - L' \frac{\partial i(z, t)}{\partial t}, \quad (2.8a)$$

$$\frac{\partial i(z,t)}{\partial z} = -G'v(z,t) - C' \frac{\partial v(z,t)}{\partial t}. \quad (2.8b)$$

These transmission line equations in the time domain are also known as the *telegrapher's equations*.

Voltage and current functions that are propagating as a sine wave in z direction can be expressed with a cosine function as:

$$v(z,t) = V_z \cos(\omega t + \varphi) = V_z \Re\{e^{j(\omega t + \varphi)}\} \quad (2.9a)$$

and

$$i(z,t) = I_z \cos(\omega t + \varphi) = I_z \Re\{e^{j(\omega t + \varphi)}\}, \quad (2.9b)$$

where V_z and I_z are the z dependent components of amplitudes, ω is the angular frequency of the steady-state wave and φ is the phase reference of the wave.

Now the sinusoidal steady-state analysis can be applied, which significantly simplifies the solving of the equations. Using the *phasor transform* [2, 3] \mathbf{P} for real parts of voltage and current wave functions:

$$V(z) = V_z e^{j(\omega t + \varphi)} = \mathbf{P}\{V_z \cos(\omega t + \varphi)\}, \quad (2.10a)$$

$$I(z) = I_z e^{j(\omega t + \varphi)} = \mathbf{P}\{I_z \cos(\omega t + \varphi)\}, \quad (2.10b)$$

the telegrapher's equations (2.8a) and (2.8b) will be transferred to the frequency domain:

$$\frac{dV(z)}{dz} = -R'I(z) - L' \frac{dI(z)}{dt}, \quad (2.11a)$$

$$\frac{dI(z)}{dz} = -G'V(z) - C' \frac{dV(z)}{dt}. \quad (2.11b)$$

With

$$\frac{dV(z)}{dt} = \frac{d}{dt} V_z e^{j(\omega t + \varphi)} = j\omega V_z e^{j(\omega t + \varphi)} = j\omega V(z) \quad (2.12a)$$

and

$$\frac{dI(z)}{dt} = \frac{d}{dt} I_z e^{j(\omega t + \varphi)} = j\omega I_z e^{j(\omega t + \varphi)} = j\omega I(z), \quad (2.12b)$$

the equations are finally simplified to

$$\frac{dV(z)}{dz} = -(R' + j\omega L')I(z), \quad (2.13a)$$

$$\frac{dI(z)}{dz} = -(G' + j\omega C')V(z). \quad (2.13b)$$

By solving both equations simultaneously

$$\frac{d^2V(z)}{dz^2} = -(R' + j\omega L') \frac{dI(z)}{dz} = (R' + j\omega L')(G' + j\omega C')V(z), \quad (2.14a)$$

$$\frac{d^2I(z)}{dz^2} = -(G' + j\omega C') \frac{dV(z)}{dz} = (G' + j\omega C')(R' + j\omega L')I(z), \quad (2.14b)$$

the *wave equations* in form of *Helmholtz equations* [2,4] for voltage and current are obtained:

$$\frac{d^2V(z)}{dz^2} - \gamma^2 V(z) = 0, \quad (2.15a)$$

$$\frac{d^2I(z)}{dz^2} - \gamma^2 I(z) = 0, \quad (2.15b)$$

with

$$\gamma = \alpha + j\beta = \sqrt{(R' + j\omega L')(G' + j\omega C')} \quad (2.16)$$

the frequency dependent complex propagation constant, which real part is the attenuation constant α and the imaginary part is the phase constant β . The same result can be obtained pure mathematically applying the separation of variables to (2.8a) and (2.8b) to solve the differential equations, though it is less “demonstrative” from the point of view of the analyzing of the wave functions.

General solutions for travelling waves of voltage and current are the sums of forward and backward travelling waves:

$$V(z) = V_z^+ e^{-\gamma z} + V_z^- e^{\gamma z}, \quad (2.17a)$$

$$I(z) = I_z^+ e^{-\gamma z} + I_z^- e^{\gamma z}, \quad (2.17b)$$

where $e^{-\gamma z}$ and $e^{\gamma z}$ terms represent wave propagation in positive and negative z direction respectively. Now solving (2.13a) with the voltage from (2.17a)

$$\frac{d}{dz} (V_z^+ e^{-\gamma z} + V_z^- e^{\gamma z}) = -(R' + j\omega L')I(z) \quad (2.18)$$

with

$$\frac{d}{dz} (V_z^+ e^{-\gamma z} + V_z^- e^{\gamma z}) = \gamma (V_z^- e^{\gamma z} - V_z^+ e^{-\gamma z}), \quad (2.19)$$

we obtain the current on the line:

$$I(z) = \frac{\gamma}{R' + j\omega L'} (V_z^+ e^{-\gamma z} + V_z^- e^{\gamma z}). \quad (2.20)$$

Thus the *characteristic impedance* Z_0 can be calculated to

$$Z_0 = \frac{V(z)}{I(z)} = \frac{R' + j\omega L'}{\gamma} = \sqrt{\frac{R' + j\omega L'}{G' + j\omega C'}} \quad (2.21)$$

and has the units of resistance. It is determined only by its geometry and the material of the transmission line and is a function of frequency.

If the TEM transmission line is perfectly terminated, that is, there are no reflections from the load, the voltage to current ratio of a wave propagating along the line is constant. Otherwise when the wave reaches the load it is partly reflected and this reflected wave travels back along the line. After reaching the source it is added to the transmitted wave and the voltage to current ratio on the input of the transmission line is no more equal to the characteristic impedance; this is called the *input impedance*.

It can be seen from Equation (2.21) that the characteristic impedance increases with smaller capacitance and vice versa. Considering the separation d between the lines it means that the further the conductors are moved from each other, the smaller is the distributed capacitance and the larger is the value of characteristic impedance, see the definition of capacitance for a parallel plate capacitor:

$$C = \epsilon_0 \epsilon_r \frac{A}{d}, \quad (2.22)$$

where C represents capacitance in F, ϵ_0 is the electric constant in F/m, ϵ_r is the relative permittivity and A is the overlap area of the plates. Not only capacitance decreases, but also the distributed inductance will increase, as the opposite magnetic fields will overlap less and therefore it comes to less field cancellation between the conductors (see Figure 2.2).

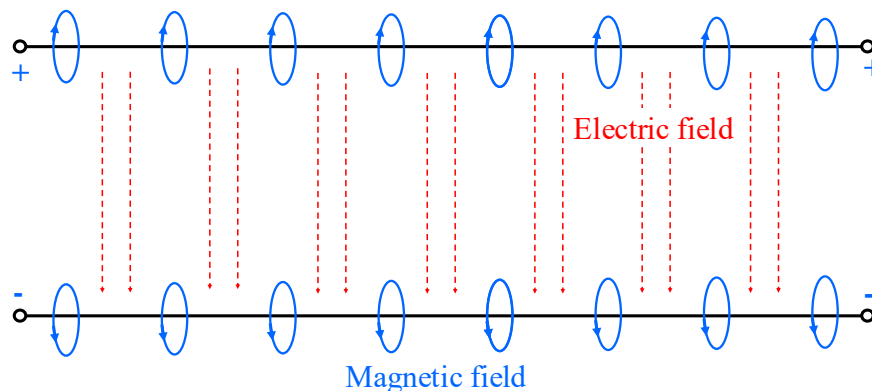


Figure 2.2: Electric and magnetic fields distribution along the transmission line.

These effects result in a smaller current drawn by the line and it leads by definition to a higher impedance. Conversely, moving the conductors closer to each other increases the current drawn from the source for any applied voltage, resulting in a smaller characteristic impedance.

Assuming the lossless line, so that any dissipative effects as conductor resistance R and dielectric losses G can be neglected, the characteristic impedance reduces to

$$Z_0 = \sqrt{\frac{L'}{C'}}, \quad (2.23)$$

and is thus purely real without reactive components.

The propagation constant becomes then

$$\gamma = \alpha + j\beta = j\omega\sqrt{L'C'}. \quad (2.24)$$

As expected for a lossless line the attenuation constant is zero.

Since the Helmholtz equations give the general solutions for a wave propagating in a lossless nonconductive medium, it can be stated, that the wave number k is equivalent to the phase constant β in case of TEM transmission lines, because the plane wave is the transversal electro-magnetic (TEM) mode of propagation. (For a waveguide, which is also a transmission line, the propagation modes are different, because waves are bounded by the waveguide walls and they are not the plane waves. Therefore the propagation constant doesn't correspond any more to the wave number, because it has not only longitudinal, but also transverse component, due to the reflection of waves from the waveguide walls.) Thus, the wavelength λ_l on the transmission line and phase velocity v_p can be found by

$$\lambda_l = \frac{2\pi}{\beta} \quad (2.25)$$

and

$$v_p = \frac{\omega}{\beta} = \lambda_l f \quad (2.26)$$

respectively. The wavelength λ_l nonmagnetic media is equal to the wavelength propagating in the vacuum reduced by the square root of relative permittivity:

$$\lambda_l = \frac{\lambda_0}{\sqrt{\epsilon_r}}. \quad (2.27)$$

2.2 Attenuation mechanisms

The general definition of the attenuation on a transmission line is given by [2]:

$$\alpha = \frac{\text{average power lost per unit length}}{2(\text{power transmitted})}. \quad (2.28)$$

Attenuation can be caused by several factors, e.g. metal conductivity, dissipation of energy in dielectric materials, dielectric conductivity, surface roughness of the metal, radiation etc. Some of them are pointed out below, as they give the biggest contribution to the transmission line attenuation.

Solving Maxwell's equations [1, 4]

$$\nabla \times \mathbf{E} = -j\omega\mu\mathbf{H}, \quad (2.29a)$$

$$\nabla \times \mathbf{H} = j\omega\epsilon\mathbf{E} + \sigma\mathbf{E} \quad (2.29b)$$

for a generally lossy medium, the following source-free Helmholtz equation is obtained:

$$\boxed{\nabla^2 \mathbf{E} = j\omega\mu(\sigma\mathbf{E} + j\omega\epsilon\mathbf{E})}, \quad (2.30)$$

Here the term $\sigma\mathbf{E}$ represents the current density and $\epsilon\mathbf{E}$ is the displacement current. Bringing the right-side term of (2.30) to the left side and rearranging the equation yields

$$\nabla^2\mathbf{E} + \omega^2\mu\epsilon\left(1 - j\frac{\sigma}{\omega\epsilon}\right)\mathbf{E} = 0. \quad (2.31)$$

Now the complex propagation constant in a lossy dielectric material [1] can be defined as

$$\gamma = \alpha + j\beta = j\omega\sqrt{\mu\epsilon}\sqrt{1 - j\frac{\sigma}{\omega\epsilon}} \quad (2.32)$$

to satisfy the wave equation.

2.2.1 Attenuation due to metal conductivity

First of all attenuation caused by metal conductivity α_c should be mentioned; while it can be neglected for low frequencies, it is the dominating part of overall transmission line loss at microwave frequencies due to the *skin effect* [1, 3]. Because of the high conductivity of the conductors, an electric field would be suppressed before reaching the core. Taking (2.32) and considering that the conduction current is much bigger than displacement current so that 1 in Equation (2.32) can be neglected, the propagation constant in a conductor is given by:

$$\gamma = \alpha + j\beta = j\omega\sqrt{\mu\epsilon}\sqrt{\frac{\sigma}{j\omega\epsilon}} \quad (2.33)$$

and can be rearranged to

$$\gamma = \alpha + j\beta = (1 + j)\sqrt{\frac{\omega\mu\sigma}{2}}. \quad (2.34)$$

It means that the attenuation and phase constants are equal and that the penetrating electric field would decay very fast in the conductor. The penetration depth or skin depth is therefore defined as an inverse of the attenuation constant:

$$\delta_s = \frac{1}{\alpha} = \sqrt{\frac{2}{\omega\mu\sigma}}. \quad (2.35)$$

with angular frequency ω in Hz, μ_0 is the permeability constant in H/m, μ_r is the relative permeability and σ is the conductivity of the metal in S. For the DC field $\omega = 0$ and the skin depth is infinitely large. The field can penetrate the whole conductor. The AC field creates eddy currents in the conductor, which leads to cancellation of the current in the core region after travelling the skin depth, see Figure 2.3. It causes the field energy to be converted into the heat.

The resistivity R is a function of metal thickness according to

$$R = \rho\frac{l}{A} = \rho\frac{l}{wt}, \quad (2.36)$$

where ρ is the bulk resistivity of the metal in Ωm , l is the length of the conductor and its cross-section A is given by product of the conductor width w and thickness t . The resistivity would increase with the frequency, because the conducting area would shrink to the skin depth. Attenuation due to conducting loss α_c is thus proportional to metal resistivity and also to the square root of frequency, see (2.36) and (2.35), because the losses are inversely proportional to the skin depth. Moreover the surface roughness can increase the specific resistivity and therefore yield a significant contribution to the attenuation of thin metal layers, which will also be discussed later in matters of the fabricated transmission lines.

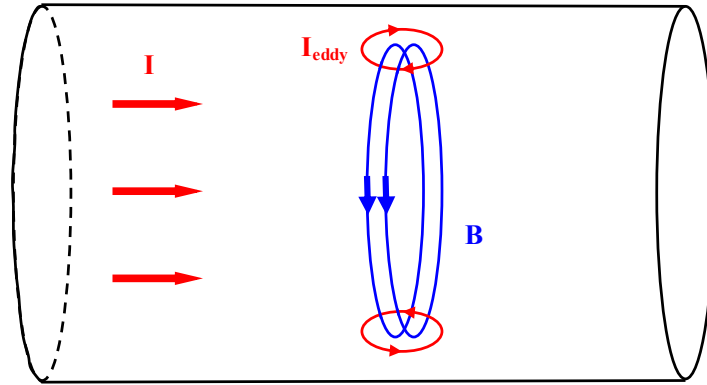


Figure 2.3: Circulating eddy currents are induced due to changing magnetic field in the conductor, weakening or cancelling alternating current in the centre of the conductor and enforcing it nearby the conductor surface. Source: Wikipedia: Skin-Effect, section “Cause”.

2.2.2 Attenuation due to the dielectric loss

Consider the displacement flux \mathbf{D} , which is given as:

$$\mathbf{D} = \varepsilon_0 \mathbf{E} + \mathbf{P}. \quad (2.37)$$

The polarization vector \mathbf{P} refers to the electric polarization of the atoms and molecules in response to the applied electric field \mathbf{E} and it is defined as

$$\mathbf{P} = \varepsilon_0 \chi_e \mathbf{E}, \quad (2.38)$$

where χ_e represents the *electric susceptibility*. Therefore displacement flux can be rewritten as

$$\mathbf{D} = \varepsilon_0 \mathbf{E} + \mathbf{P} = \varepsilon_0 (1 + \chi_e) \mathbf{E} = \varepsilon_0 \varepsilon_r \mathbf{E} = \varepsilon \mathbf{E}, \quad (2.39)$$

where ε_r is the relative permittivity and ε is the absolute permittivity of the medium. The electric susceptibility is complex. But the complex part is as a rule neglected since it develops only at high frequencies. This is due to two various kinds of polarization mechanisms. The first one accounts to the formation of dipole moment by the negatively charged electron cloud and the positively charged atomic nucleus in presence of an electric field [5]. The second mechanism is the orientation polarization, which aligns dipoles according to the applied electric field. For microwave frequencies, the relaxation processes of the orientation polarization plays a significant role. This relaxation time causes some phase shift between

the electric field phasor and polarization density phasor, thus the electric susceptibility and permittivity become complex quantities:

$$\mathbf{D} = \varepsilon_0 \mathbf{E} + \mathbf{P} = \varepsilon_0 (1 + |\chi_e| e^{-j\alpha}) \mathbf{E} = \varepsilon_0 (1 + \chi'_e - j\chi''_e) \mathbf{E}. \quad (2.40)$$

Comparing (2.40) with (2.39) shows that the term in brackets represents the relative permittivity. Therefore the absolute permittivity is given by

$$\varepsilon = \varepsilon' - j\varepsilon'' = \varepsilon_0 (\varepsilon'_r - j\varepsilon''_r), \quad (2.41)$$

and it can be seen that the term ε''_r represents the losses due to the alternating electrical field. Since we are still discussing the lossy dielectric medium, there is some conducting current given by Ohm's Law:

$$\mathbf{J}_c = \sigma \mathbf{E}. \quad (2.42)$$

The displacement current

$$\mathbf{J}_d = j\omega \varepsilon \mathbf{E} = j\omega (\varepsilon' - j\varepsilon'') \mathbf{E} \quad (2.43)$$

can be won deriving the displacement flux in frequency domain. The sum of both currents gives us the total induced current density:

$$\mathbf{J} = \mathbf{J}_d + \mathbf{J}_c = j\omega (\varepsilon' - j\varepsilon'') \mathbf{E} + \sigma \mathbf{E} = j\omega \left[\varepsilon' - j\varepsilon'' - j \frac{\sigma}{\omega} \right] \mathbf{E}. \quad (2.44)$$

Finally the specific value called *dielectric loss tangent* is obtained by

$$\tan \delta_e = \frac{\omega \varepsilon'' + \sigma}{\omega \varepsilon'}. \quad (2.45)$$

The term $\omega \varepsilon'' + \sigma$ represents the total losses, which are composed of the conductivity loss and loss arising from the dielectric dipoles forced to change their orientation constantly. For high frequencies the conductivity loss is negligible compared to the dielectric loss and therefore the loss tangent reduces to

$$\tan \delta_e = \frac{\varepsilon''}{\varepsilon'}. \quad (2.46)$$

At lower frequencies there is almost no contribution of the orientation polarization to the loss mechanism, so that relative permittivity is not a complex number. This assumption for the loss tangent is given as:

$$\tan \delta_e = \frac{\sigma}{\omega \varepsilon}. \quad (2.47)$$

Equation (2.32) can be rewritten using (2.47) to

$$\gamma = \alpha + j\beta = j\omega \sqrt{\mu \varepsilon} \sqrt{1 - j \tan \delta_e} \quad (2.48)$$

for low frequencies. Further the losses due to the dielectric can be derived. All the terms are brought under the square root:

$$\sqrt{(\alpha + j\beta)^2} = \sqrt{-\omega^2\mu\epsilon(1 - j\tan\delta_e)}, \quad (2.49)$$

$$\sqrt{\alpha^2 + 2j\alpha\beta - \beta^2} = \sqrt{-\omega^2\mu\epsilon - j\omega^2\mu\epsilon\tan\delta_e}. \quad (2.50)$$

Comparing the imaginary parts, which represent dielectric loss as derived above, this dielectric loss or so called dissipation factor α_D can be estimated as follows:

$$\alpha_D = \frac{\omega^2\mu\epsilon\tan\delta_e}{2\beta}. \quad (2.51)$$

Here μ is the product of the permeability constant in vacuum μ_0 in H/m and the dimensionless relative permeability μ_r in the material. This is legit in an analogous way for the permittivity: it is the product of permittivity constant of vacuum permittivity ϵ_0 in F/m and the relative permittivity ϵ_r of the material. The phase constant can be written in terms of the phase velocity using

$$\beta = \frac{\omega}{v_p}. \quad (2.52)$$

Phase velocity describes the speed of propagating electromagnetic waves in a medium and is smaller by the factor of $\sqrt{\mu_r\epsilon_r}$ than the speed of light,

$$\beta = \frac{\omega}{c}\sqrt{\mu_r\epsilon_r}. \quad (2.53)$$

The speed of light is in its turn defined as the speed of an electromagnetic wave propagating in vacuum:

$$c = \frac{1}{\sqrt{\mu_0\epsilon_0}}. \quad (2.54)$$

The propagation constant is obtained as follows:

$$\beta = \omega\sqrt{\mu_0\epsilon_0\mu_r\epsilon_r} = \omega\sqrt{\mu\epsilon}. \quad (2.55)$$

With Equation (2.55) the dissipation factor becomes:

$$\alpha_D = \frac{\omega\sqrt{\mu_0\epsilon_0\mu_r\epsilon_r}\tan\delta_e}{2}, \quad (2.56)$$

using Equation (2.54) and applying the relative permeability of a non-magnetic medium as 1, α_D is finally reduced to

$$\alpha_D = \frac{\pi f\sqrt{\epsilon_r}\tan\delta_e}{c}, \quad (2.57)$$

and is proportional to frequency. It means that for high frequencies dielectric losses dominate ohmic losses, which are proportional to the square root of frequency. Obtaining the above discussed parameters: characteristic impedance Z_0 , the phase constant β (or as well phase velocity v_p) and attenuation constant α , any TEM mode supporting transmission line can be fully characterized.

2.3 Scattering matrix

In order to analyze fabricated transmission lines, the concept of the scattering matrix is used. It is elaborately described in [1], nevertheless it is briefly introduced in this section.

While it is highly complicated to determine voltages and currents at high frequencies, as well as to realize short and open circuits and measure the short and open circuit voltages, because the high frequency measurement equipment doesn't have sufficiently low or high input resistance, the scattering parameters offer the solution in terms of voltage waves.

Consider a two-port network as shown in Figure 2.4.

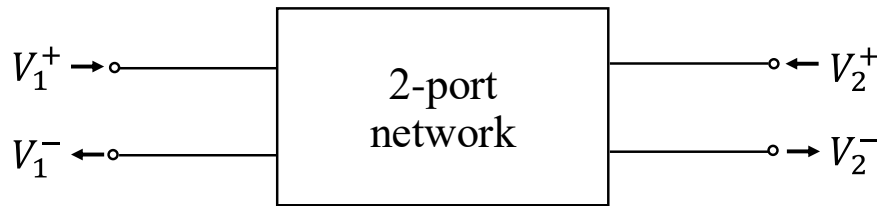


Figure 2.4: Schematic view of generalized two-port network.

The measurement and characterization of network scattering parameters is based on the ratios of the incident, reflected and transmitted voltage waves. The input and load impedances of the network analyzer are usually 50Ω and the characteristic impedance of the line should match them. The scattering matrix of the two-port network looks like presented below in (2.58):

$$\begin{pmatrix} V_1^- \\ V_2^- \end{pmatrix} = \begin{bmatrix} S_{11} & S_{12} \\ S_{21} & S_{22} \end{bmatrix} \begin{pmatrix} V_1^+ \\ V_2^+ \end{pmatrix}, \quad (2.58)$$

where:

- V_n^+ are the voltage waves moving forward,
- V_n^- are the voltage waves moving in reverse direction,
- S_{11} is the reflection r seen on port 1,
- S_{12} is the reverse transmission from port 2 to port 1,
- S_{21} is the transmission from port 1 to port 2,
- S_{22} is the reflection seen on port 2.

The S_{11} parameter is thus defined as ratio of the reflected fraction of the input voltage wave V_1^- to the incident input voltage wave V_1^+ , while there is no reflection from the output port (because of "perfect" termination). According to

$$S_{11} = r = \frac{Z_{load} - Z_0}{Z_{load} + Z_0}, \quad (2.59)$$

the characteristic impedance Z_0 of the transmission line can be calculated after scattering parameter measurements with known load impedance Z_{load} and measured reflection parameter. In case of a no-perfectly matched output (some reflection occurs), this reflected wave fraction travels back to the input port and is added to the input wave. Thus, the impedance

seen on the input is no more the characteristic impedance of the line, but the *input impedance* Z_{in} .

The forward transmission S_{21} is given by the ratio of the voltage wave reflected at the output side and the incident wave on the input side, again without consideration of mismatch loss, so that the transmission line on the input is matched perfectly without reflections. Generally each specific element of the scattering matrix is given by:

$$S_{ij} = \left. \frac{V_i^-}{V_j^+} \right|_{V_k^+ = 0 \text{ for } k \neq j} \quad (2.60)$$

The scattering parameters can be represented linearly, but for the sake of convenience they are mostly plotted in dB, which is illustrated later discussing the fabricated transmission line characteristics. Both reflection parameters S_{11} and S_{22} can be represented in a Smith chart and the transmission parameters S_{12} and S_{21} in a polar diagram, as shown in Figure 2.5.

The Smith chart is explained in detail in [1]. The Smith chart is a chart of normalized impedances, so that the impedance of the reflection parameters can be read out at every point on the chart. If the reflection is normalized to the generator impedance, it could be easily seen how good the input impedance of the transmission line is matched to the generator impedance. In the Smith chart the point in the center of the circle indicates the perfect match of the generator and characteristic impedance, which means zero reflection (and in the polar diagram the center point indicates zero transmission). At the outmost circle the reflection is maximum, i.e. 1 (in the polar diagram it gives the maximum transmission). If there is some circle of reflection with certain radius and the center point placed on the real (horizontal) axis, the reflection magnitude is equal to its radius and is thus constant. Moreover the phase is moving along the radius of the reflection circle in clockwise direction; the same holds for the polar diagram. Additionally, the type of the reactance can be read: for the impedance coordinates, while the horizontal axis is the real axis corresponding to the resistance, the upper plane above the real axes of the chart represents inductive reactance and the plane under the real axes represents capacitive reactance. For the admittance coordinates inductive and capacitive reactance are swapped. It is possible to adapt the circuit characteristics to needed values, e.g. if there is some unwanted inductivity it is easy to calculate the required capacitance value using the Smith chart to cancel the inductivity and provide purely real impedance. The very right and left points on the real axis indicate the open and the short circuit respectively.

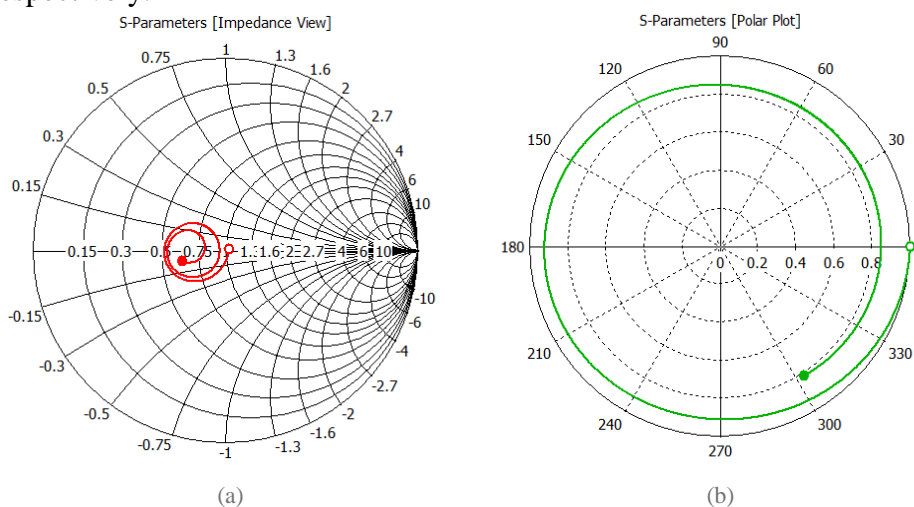


Figure 2.5: for the sake of example represented (a) S_{11} parameter from CST MWS[®] simulations on Smith chart and (b) S_{21} parameter on the polar diagram.

Figure 2.5 (a) is given as example: the curve starts close to 1 in the center of the Smith chart, which means that there is some reflected fraction of the voltage wave, but still the impedance is very close to the generator impedance. Traveling along the curve with growing frequency, the impedance values are shifted further from the center, and additionally there are portions of inductive or capacitive reactance. On the polar diagram in Figure 2.5 (b) the transmission curve starts at zero phase angle from the maximum point at the outer circle. It travels with growing frequency in clockwise direction. At the end point, i.e. at with the maximum frequency, the transmission is 20 % less than at the start point. Taking the frequency range into account, it can indicate, for example, that the bandwidth of the transmission line or transmission line circuit is small, so that it can be used only for a small frequency range. However broadband devices are usually preferred.

2.4 Coplanar waveguide

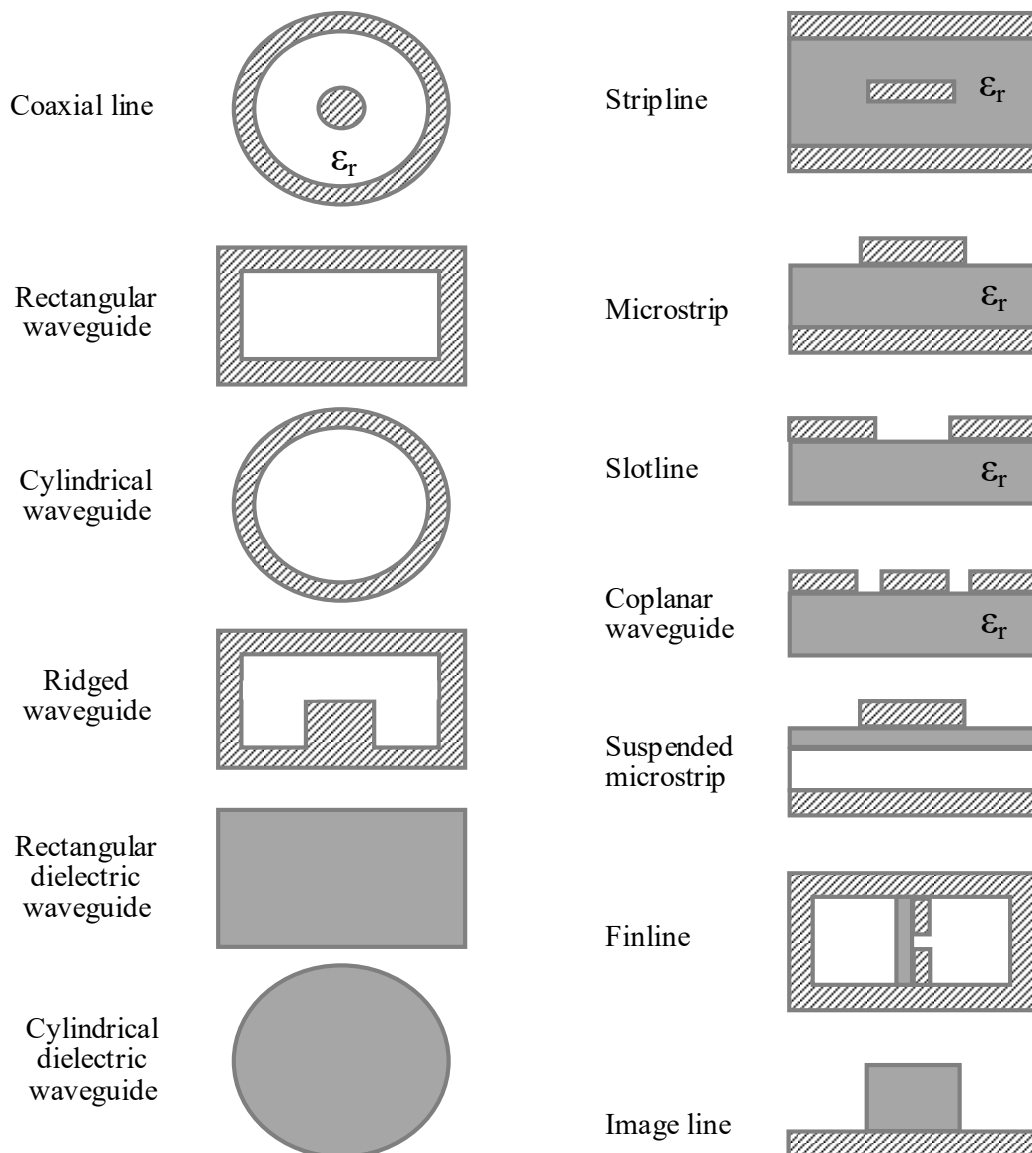


Figure 2.6: Transmission line structures. Source: [1]

Due to the large range of application fields in the micro- and millimetre wave domain, there are a lot of variations of microwave transmission line designs. Cross-sectional views of most used are presented in Figure 2.6. Transmission line structures can be a conventional metallic waveguides or coaxial lines. Transmission line structures can be integrated planar structures, which are being intensively developed in the recent years for the sake of miniaturizing the circuits, for example strip or microstrip lines or even multi-line structures like slot lines, coplanar waveguides or their coupled variations, that can be fabricated “on chip”.

During this thesis coplanar waveguides [5, 6] are designed and fabricated and therefore the fundamentals of this type of transmission lines are presented in this section.

The electric field lines of even mode of the CPW (coplanar waveguide) start on the center conductor and end on the surrounding ground planes. The electric and magnetic field distribution are shown in Figure 2.7:

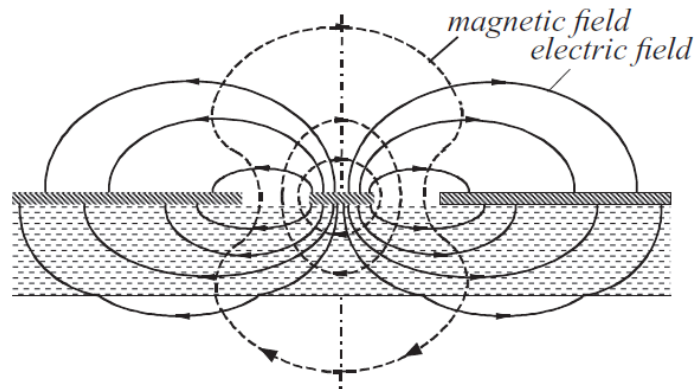


Figure 2.7: Electric and magnetic field distribution of the even mode on a CPW. Source: [6]

Another one mode, which could propagate along the CPW, if the ground planes are not kept on the same potential, is an odd mode. It is the normal propagation mode of a slot line, which has only two conducting strips separated by slot. Hence the field lines would start on the one ground and end on the opposite ground, barely touching or avoiding the conducting strip, and spread much further from the edges of the grounds than the field lines of even mode [6], which influences the propagation constant. This mode is not discussed further. The following analysis of the measured transmission lines in Chapter 6 shows that the propagation constant of the simulated and fabricated transmission lines are in good agreement, which excludes a transition of even mode into odd mode along the line.

The big advantage of the CPW for a given substrate is that it has two parameters to adjust which control the impedance: the strip width W_{strip} and the spacing width W_{space} (see Figure 2.8), in contrast to, for example, the microstrip line, where only the strip width can be optimized.

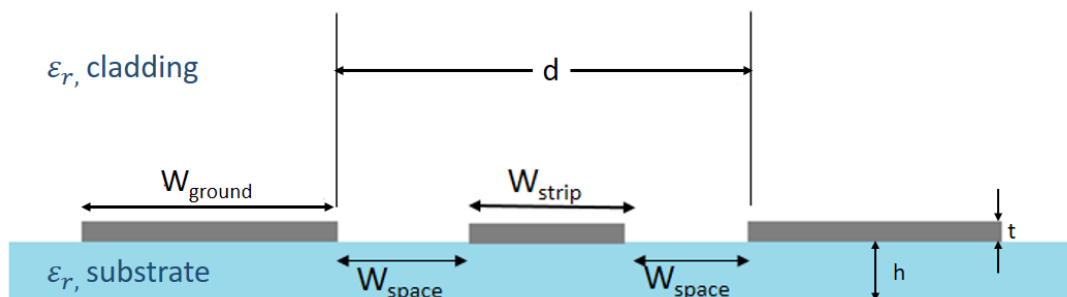


Figure 2.8: Schematic view of the coplanar waveguide.

The effective dielectric constant $\varepsilon_{r,eff}$ of the coplanar waveguide is defined as the composition of both the substrate and cladding (air or dielectric material) relative dielectric constants. At low frequencies the field lines are distributed more or less equally in the substrate and in the cladding and therefore the effective dielectric constant of a lossless line represents the arithmetic average value of both the dielectric constants. For high frequencies more lines would migrate to the material with larger permittivity, e.g. to the substrate in case of air cladding. Therefore the value of the effective permittivity would be closer to the value of permittivity of substrate. Nevertheless the effective dielectric constant and characteristic impedance doesn't change much within the quite broad frequency range if the coplanar waveguide is designed properly; thus the propagation even mode which is supported by the CWP has low dispersion and in good approximation can be considered as quasi-TEM mode. In this way all the theory described in previous sections is applicable.

Below formulas from [7] are written, that allow the calculation of the characteristic impedance and effective dielectric constant for a coplanar waveguide in good approximation. Nevertheless the calculations are completely frequency independent, thus assuming a non-dispersive behavior.

$$Z_0 = \frac{30\pi}{\sqrt{\varepsilon_{r,eff,t}}} \cdot \frac{K(k'_t)}{K(k_t)}, \quad (2.61)$$

$$\varepsilon_{r,eff,t} = \varepsilon_{r,eff} - \frac{\varepsilon_{eff}^{-1}}{\frac{(d-W_{strip})/2}{0.7t} \cdot \frac{K(k)}{K'(k)} + 1}, \quad (2.62)$$

$$\varepsilon_{r,eff} = 1 + \frac{\varepsilon_r - 1}{2} \cdot \frac{K(k')K(k_l)}{K(k)K(k'_l)}, \quad (2.63)$$

where :

$$k = \frac{W_{strip}}{d}, \quad (2.64) \quad k_t = \frac{W_{strip,t}}{d_t}, \quad (2.65)$$

$$k' = \sqrt{1 - k^2}, \quad (2.66) \quad k'_t = \sqrt{1 - k_t^2}, \quad (2.67)$$

$$k_l = \frac{\sinh\left(\frac{\pi W_{strip,t}}{4h}\right)}{\sinh\left(\frac{\pi d_t}{4h}\right)}, \quad (2.68) \quad k'_l = \sqrt{1 - k_l^2}, \quad (2.69)$$

$$W_{strip,t} = W_{strip} + \frac{1.25t}{\pi} \left[1 + \ln\left(\frac{4\pi W_{strip}}{t}\right) \right], \quad (2.70)$$

$$d_t = d - \frac{1.25t}{\pi} \left[1 + \ln\left(\frac{4\pi W_{strip}}{t}\right) \right]. \quad (2.71)$$

K and K' are here the complete elliptic functions of the first and kind [8] given by:

$$K(m) = \int_0^{\pi/2} (1 - m \cdot \sin^2 \theta)^{-1/2} d\theta \quad (2.72)$$

and

$$K(m_1) = K(1 - m) = \int_0^{\pi/2} (1 - m_1 \cdot \sin^2 \theta)^{-1/2} d\theta \quad (2.73)$$

3 Atomic vapor cell

Although experiments with atomic vapor cells is not an objective of this thesis, a superficial overview of the working principle, application and structure of the vapor cell is presented in this chapter with the aim to provide the reasoning for its use and to present its advantages. The detailed discussion of all the processes, calculations and data is to be found in [9].

3.1 Fundamentals of the rubidium vapor cell

Motivation

The 5th Institute of Physics in cooperation with the Institute for Large Area Microelectronics has been researching in the field of quantum computing and atom-based electric field sensing. Alternatively to the systems like quantum dots or trapped ions and atoms, Rydberg atoms can be used for quantum information processing [9, 10]. While the quantum logic gates with Rydberg atoms were already demonstrated in ultra-cold experiments [11, 12], the next step would be to apply this principle at room temperature. There are already alkali vapor cells at and above room temperature which are used for magnetometry and magnetic and electric field sensing and some of them already reached industrial level. They are based on atoms in low excited states. Atoms in highly excited states like Rydberg atoms offer much higher sensitivity. However a low background pressure is necessary for Rydberg spectroscopy. Several cell fabrication techniques for atomic vapor cell fabrication were developed at the 5th Institute of Physics. The most suitable technique for thin cells is discussed below. Obtaining such a cell allows investigation of the behavior of alkali atoms excited to the Rydberg state. This approach promises a range of possibilities for quantum computing, that could replace state-of-the-art classical computation with much faster computation time and higher energy efficiency. It can also be applied for atom-based electric field sensing. The huge advantage of such a detector is that there is no need for calibration as the natural constants are the base for the detection system. This means great accuracy and reproducibility of the device. Furthermore antennas, which are usually used in such cases, are made of metals and disturb the field of the structures that have to be tested, while atoms do not influence the field. Small distortions can be provided by the cell and the interaction of the Rydberg atoms with the cell walls should therefore be investigated more carefully.

Rydberg atoms

Rydberg atoms have at least one electron in a state with a high principal quantum number. By approximation, to the Rydberg state excited alkali atoms, which have one valence electron, can be treated as hydrogen-like atoms. The most important feature of the Rydberg states is the large orbital radius and therefore large dipole moment. It offers the advantage of high polarizability, which makes the Rydberg atoms extremely sensitive to electric fields. In combination with the relatively long lifetimes, Rydberg atoms are perfect candidates for field sensing applications, for example to characterise small circuits or metamaterials. It is often difficult to use an antenna for this purpose, either because it disturbs a field that has to be

measured or even geometrically. As already mentioned, they also promise high potential for quantum computing applications.

Cell construction

Some special conditions have to be fulfilled for experiments with Rydberg atoms. First of all they require low pressure. To provide high transparency for laser light and also high mechanical stability regarding temperature changes or gradients, borosilicate or quartz glass are used for the cells. Regarding these conditions the cell fabrication method based on glass-to-glass anodic bonding is used at the 5th Institute of the Physics to bond the glass substrates on the top and on the bottom of the glass frame, as presented in Figure 3.1. This sealing method will be described in the next section of this chapter.

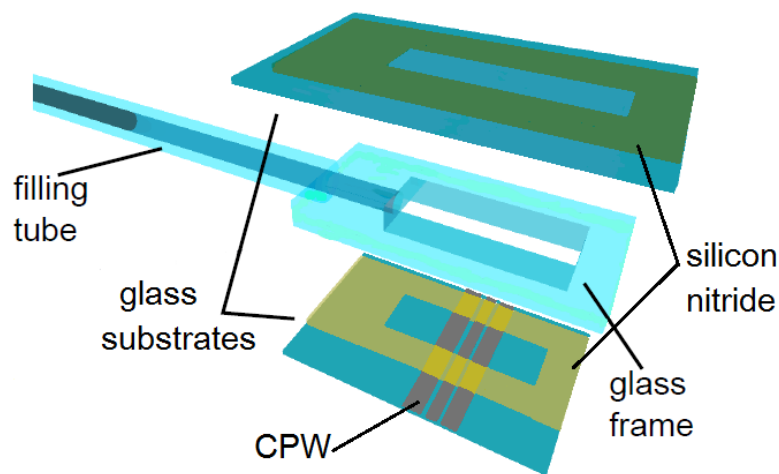


Figure 3.1: Schematic view of an atomic vapor cell. The glass frame is hermetically sealed with glass substrates. The tube with rubidium is connected to the frame.

The cell consists of a cuboid cavity connected to a filling tube, which serves as a reservoir for rubidium, see Figure 3.1. Metallic layers can be structured on the glass substrates. For example, the CPW designed in this thesis are deposited on the glass wafer. On both glass substrates, a silicon nitride layer is deposited as it is required for anodic bonding. The glass frame and both top and bottom glass plates are sealed simultaneously to form a hermetic chamber. In order to fill the vapor cell with rubidium, the filling tube is connected to a glass manifold. The vacuum turbo pump is attached to one end of the manifold, which evacuates the cell to a pressure under 10^{-6} mbar for two days, while the cell is heated to 120°C . The temperature of the reservoir defines the vapor pressure in the cell and is kept lower than the temperature of the cell to avoid condensation of rubidium in the cell. After this, the breakseal ampoule with rubidium in the other junction of the manifold is broken with the steel sphere. It allows the rubidium to fill the cell. Subsequently, the vapor cell is pumped and heated for several days, and finally, the filling tube is melted off the cell, thus sealing it. The setup is schematically presented in Figure 3.2. During this work, however, only the bottom glass plate was bonded to the glass frame to test the bonding process itself and to make electrical measurements on the coplanar waveguides after bonding.

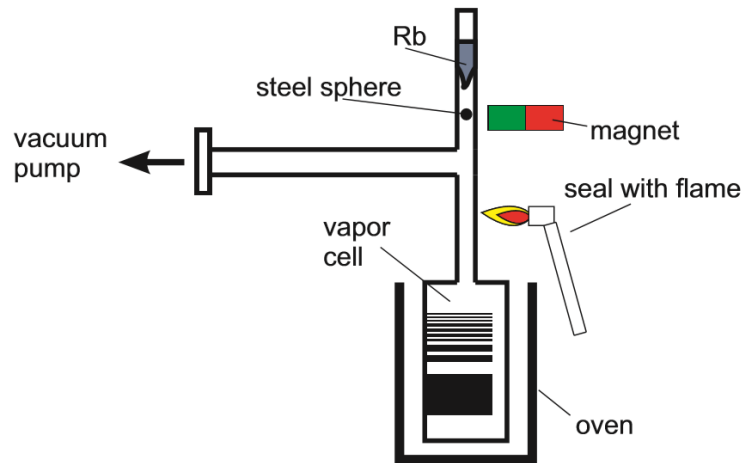


Figure 3.2: Schematic view of the setup. A vacuum pump creates a pressure of $< 10^{-6}$ mbar. Afterwards magnet and steel sphere open the breakseal ampoule and the vapor cell is filled with liquid rubidium. Eventually the connection tube is sealed off with a flame. *Source:* [9]

Atom based electric field detection

The technology for radio frequency (RF) with extension to far infrared (FI) electric field sensing based on quantum interference of Rb atoms is proposed in [10]. These atoms excited to the Rydberg states are prepared in the vapor cells in a gas phase. The working principle of the sensor is based on optical detection of Rydberg atoms using electromagnetically induced transparency (EIT). The atoms in the vapor cell represent the coherent quantum interferometer with two laser fields aligned in counterpropagating direction applying EIT. The three-level system shown in Figure 3.3(a) helps to describe the process. The weak resonant probe laser couples the ground state of Rb atoms to the second excited state and is therefore absorbed, see the bottom graph in Figure 3.3(b). When an intense coupling laser excites the atom to the Rydberg state, the eigenstate of the three-level system effectively splits into two new eigenstates. The cause of that is the fact, that the atom can be excited in two ways. The simpler one is the transition from the ground state to the second excited state. More complex possibility is to excite the atom directly to the state and then de-excite it to the second excited state by stimulated emission. Both pathways have their own complex probability density which can be calculated and which are destructively superposed. Hence, the probe and coupling beam create a quantum interference in the atom and a spectrally narrow transparency window opens on resonance because the atom becomes transparent to the probe laser fields. This phenomenon is referred to as EIT. It is also called dark resonance or dark state because the normally absorbing matter no longer absorbs the probe light. The middle graph of Figure 3.3(b) shows the transmission of the probe laser during its scanning in presence of the coupling laser. When applying an RF-FI electric field that is resonant with the third transition it changes the interference in the atom and creates a narrow absorption valley, see the lower transmission graph of Figure 3.3 (b). This process is called bright resonance because the EIT phenomenon responsible for the transmission of light now absorbs light. The detection setup is schematically presented in Figure 3.4. The probe beam goes through the cell to the detector. The coupling beam is aligned in counterpropagating direction to the probe beam. An electric field is provided by a horn antenna under the cell.

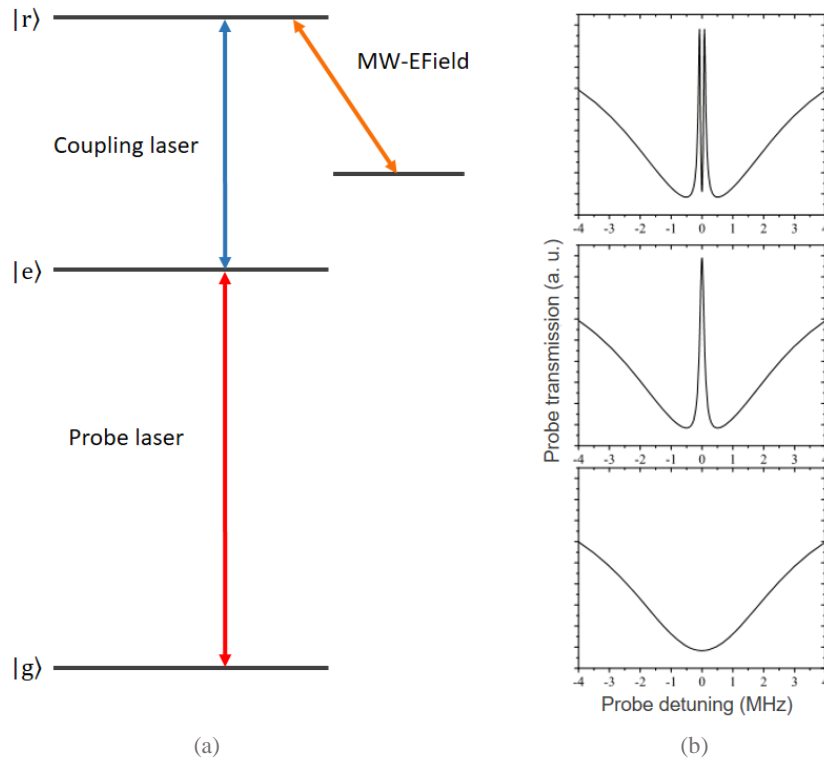


Figure 3.3: Three-level system for the excitation of Rb atoms to the Rydberg state (a) with corresponding optical transitions (b). In the first step the atom in ground state is excited with the resonant probe laser. The resulting absorption spectrum is plotted in the lower graph. By turning the resonant coupling laser on the atom is excited to the Rydberg state and a small transmission window appears in the probe laser spectrum, as plotted in the middle graph. The upper graph shows the transmission spectrum if an electric field is applied, which is resonant to the coupling laser. In this case a narrow absorption dip is created within the EIT transmission window. Source: [9]

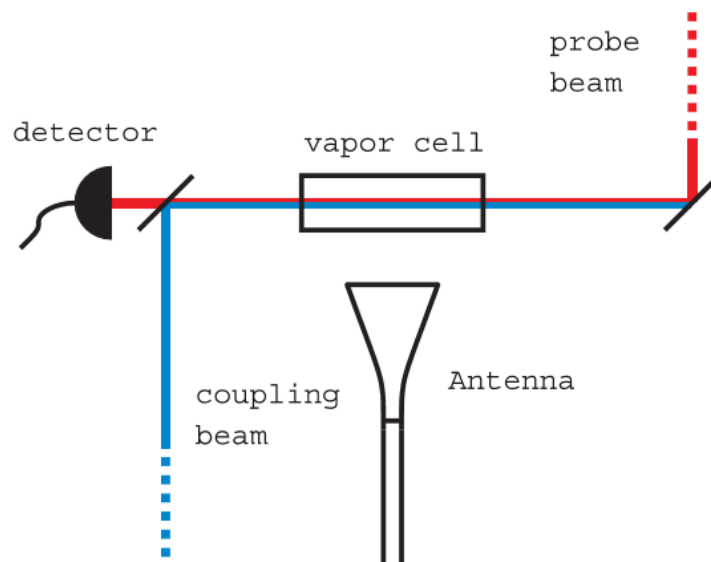


Figure 3.4: The experimental setup for electric field sensing. Source: [9]

3.2 Glass-to-glass anodic bonding

There are several variations of glass-to glass anodic bonding techniques for sealing vapor cells regarding the materials of intermediate layers [9, 13.]. For example nonconductive or conductive materials can be used. In this section the bonding method is described, which is used to bond the glass frame to the glass substrate with the coplanar waveguides fabricated on it during this thesis.

The principle of the anodic bonding technique relies on a diffusion processes resulting from an applied high voltage. It is the most advantageous method to hermetically seal vapor cells. Other possibilities are glass-blown or glued cells. In the first case there is no way to integrate metal structures inside the cell. The drawback of the second alternative is the pretty high outgassing rate of the glue. Other advantages of anodic bonding are relatively low operating temperature of around 300 – 500°C, a decisive feature for keeping metal structures undeformed, and the long-term pressure stability. In any case only the anodic bonding is suitable for the thin cells fabrication.

To permanently join two glass wafers they are placed in stack on the hotplate, see Figure 3.5. Borosilicate glass is used because it contains mobile charges when heated to the process temperature of 300°C. Another metal plate is put on top and is used as cathode, while the

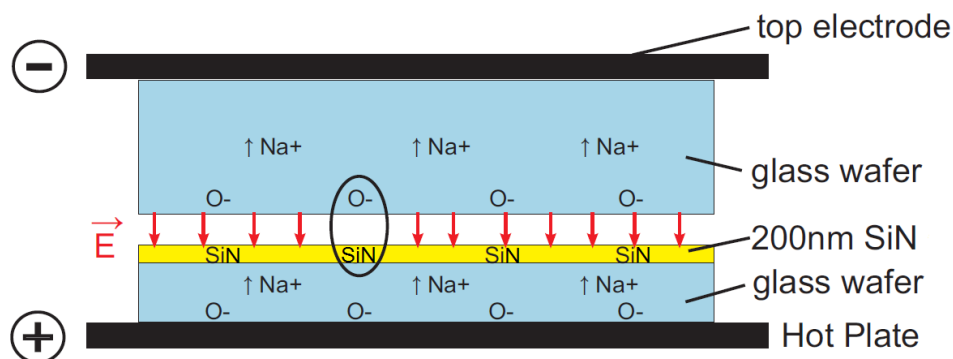


Figure 3.5: Glass-to-glass anodic bonding with an intermediate SiN layer. The intermediate layer acts as a diffusion barrier for the sodium ions. Furthermore, the silicon atoms from the intermediate layer are needed to bond the upper glass wafer. *Source:* [9].

hotplate is the anode of the arrangement. The whole stack is homogenously heated; the sodium ions become mobile at a temperature of 300°C. After reaching the operating temperature a voltage of 900 V is applied. It forces the mobile sodium ions from both substrates to move towards the cathode. The intermediate silicon nitride layer, which acts as a diffusion barrier prevents the sodium ions from the bottom substrate from reaching the top substrate. Thus the sodium ions diffuse much slower through the SiN layer than through glass and this results in the accumulation of positive charges at the interface from the lower substrate side. The oxygen ions in their turn are less mobile and stay bonded to the silicon-oxide structure of the glass. In this way a negatively charged depletion region is formed in the glass on the side of the upper substrate. The electric field resulting from these charges pulls the two substrates together into close contact. The oxygen atoms with open bonds, which are left behind from the sodium ions, react with the silicon of the SiN layer forming silicon dioxide layer and creating thereby a strong molecular bond.

The surface contact happens during the first seconds under voltage. Approximately 20 minutes are needed to build the molecular bond. After that, the voltage is turned off and the stack is slowly cooled down to avoid a thermal shock of the glass.

In a similar way, simultaneous double-side anodic bonding can be realised to seal the cell in one step. The schematic set up is shown in Figure 3.6. In this case two glass substrates are bonded to the glass frame from both sides to form the vacuum cell. This method is currently used at the 5th Institute of Physics and is described in detail in [14].

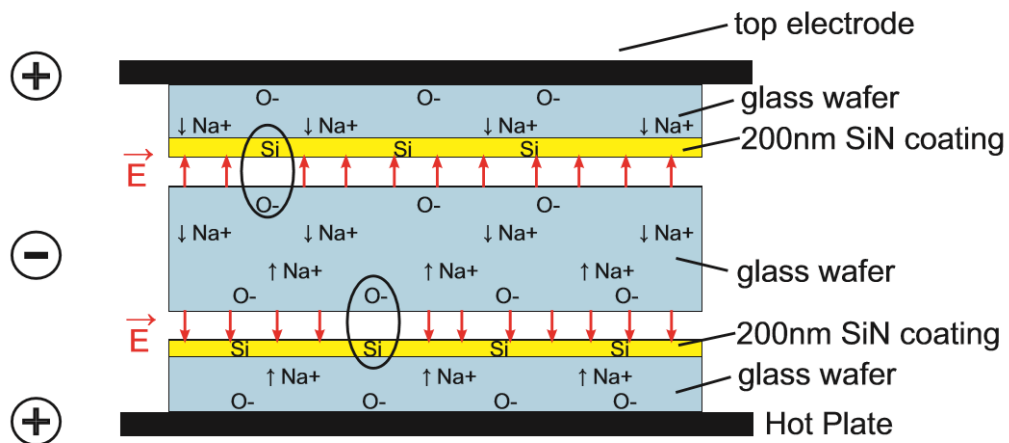


Figure 3.6: Simultaneous double-side glass-to-glass anodic bonding. The bottom and the top electrode are on the same positive potential. The middle substrate is on a negative potential. Simultaneous bonding with equal bond strength on both sides can be achieved. *Source:* [9].

When using successive anodic bonding, the bonding process of the second side destroys or at least weakens the first bond, because a reversal of the first bonding voltage is applied. This method is therefore not suitable for the aimed cell performance and the successive anodic bonding of three glass substrates is preferred. Here both the hotplate and upper metal plate are grounds and the middle substrate is negative with respect to GND. The outer substrates are coated with silicon nitride like in the double-stack case. Sodium ions diffuse from both outer sides to the middle substrate, which is enclosed by metallic wire acting as an electrode.

4 Design and simulation of transmission lines

For the integration of the transmission lines into the vapor cell, a coplanar waveguide is chosen. It offers a convenient solution considering the available laboratory equipment and contacting issues. Another possibility are the microstrip lines, but then an additional fabrication step is needed to deposit a metal layer for ground and another step to connect ground with the signal conductor. Besides, back grounded structures like microstrip lines can support coupling into the substrate which leads to higher losses. For the transmission lines that should be designed during this thesis, every additional dissipation source should be avoided due to their critical length.

Simulations were done in the software laboratory of the Institute of Electrical and Optical Communications Engineering (INT). When simulating with CST MICROWAVE STUDIO® several difficulties arose. Regarding future cell sealing an intermediate bonding layer (see section 3.2.) should be deposited on the glass substrate above the CPW. Usually conductive materials are preferable because they have better performance [13]. Firstly simulations with aluminum above the CPW were done presented in Figure 4.1. The dielectric layer should not exceed 200 nm as a thin cell is wanted, while the spacing between the metal lines is in μm scale. In this case the isolation is insufficient and the E-field is between the signal line of the CPW and the bonding layer which causes significant leakage current between them. Hence, an aluminum bonding layer is not used and only silicon nitride is left for the subsequent bonding process.

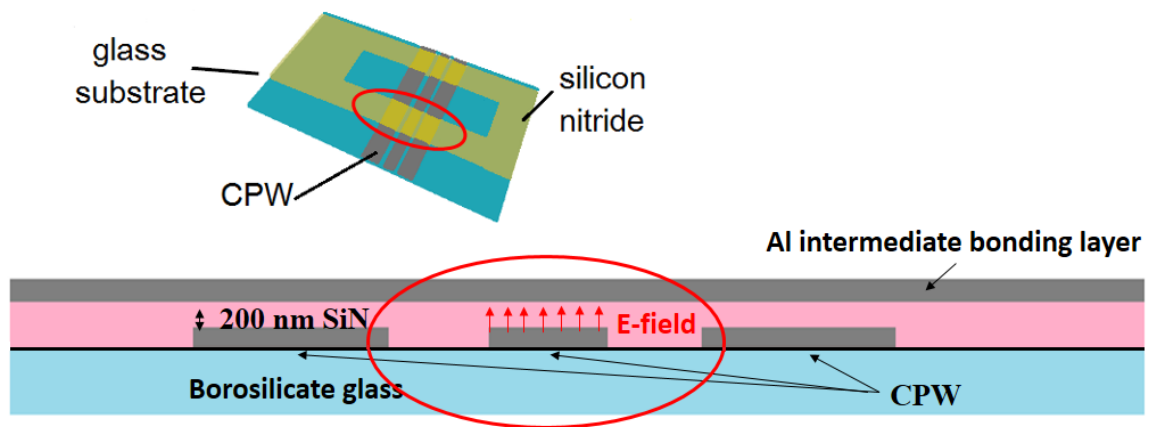


Figure 4.1: Schematic (not to scale) view of the bottom glass substrate to be bonded on the glass frame with a CPW structure on it.

The biggest challenge in this work is the geometry of the CPW, which is defined by the vapor cell size. As mentioned, only thin film layers are considered, therefore the metallization thickness should not exceed 50 nm. In addition the CPWs have to cross the cell along the whole width of 2 cm and 1 cm more from each side, see Figure 4.2. The length of the transmission lines is therefore 4 cm, which is difficult to simulate due to restricted storage space and the need of a sufficient mesh quality. As the glass substrate with the CPWs should be late bonded to the glass frame, it means that there silicone dioxide cladding will be formed where CPWs overlap with frame. So these sections also should be simulated and matched to the impedance of the CPWs under air cladding.

It is difficult to predict the behavior of such a long structure, therefore several reference CPWs with slightly different spacing widths W_{space} and strip width W_{strip} are fabricated. According to Figure 4.4 the distance d between inner edges of ground strips is fixed to 260 μm

due to the available 3-pins microwave coplanar probes. The distance between two neighboring pins (ground-signal) is $150\ \mu\text{m}$, therefore the distance between two outer pins is $300\ \mu\text{m}$. $20\ \mu\text{m}$ for pins per se at each side are left. The probe is presented in Figure 4.3.

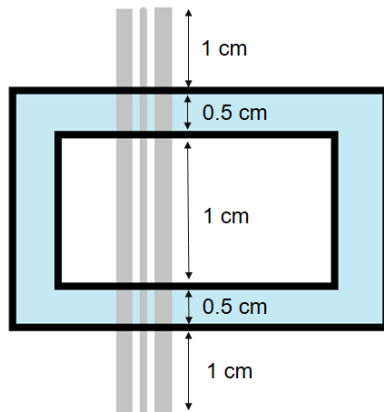


Figure 4.2: CPW under the frame, schematic.

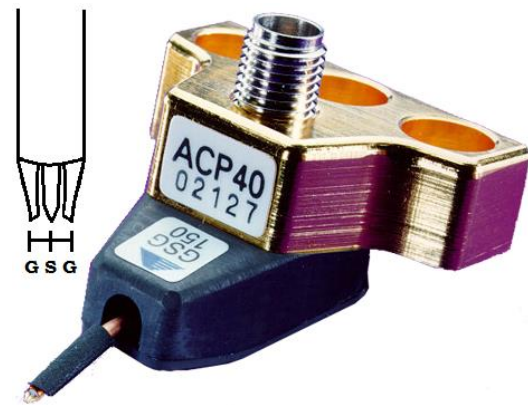


Figure 4.3: Microwave coplanar probe.

The resulting coplanar waveguide cross-section is presented in Figure 4.4.

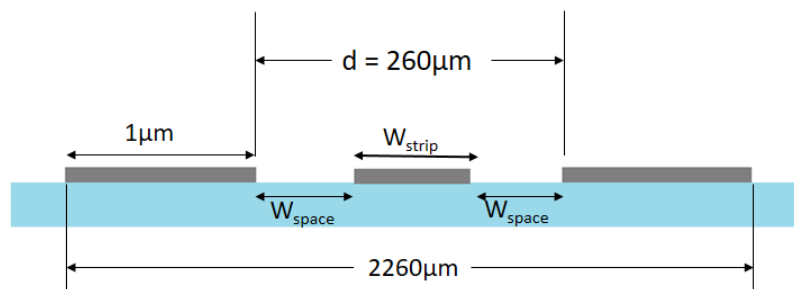


Figure 4.4: Coplanar waveguide designed for fabrication, schematic view.

Varying the strip and spacing width, 6 reference CPWs are defined, which should provide approximately $50\ \Omega$ to $100\ \Omega$ impedance. They are listed in Table 4.1 along with the simulated impedance values and calculated analytically ones for air cladding using formulas described in section 2.4. The formulas for analytic calculation are approximation which are frequency independent and don't consider material properties like specific conductivity. Short $0.5\ \text{cm}$ CPWs are simulated with air and SiO_2 cladding at $100\ \text{MHz}$ in order to get the characteristic impedances.

$W_{\text{strip}}\ [\mu\text{m}]$	$W_{\text{space}}\ [\mu\text{m}]$	$Z_{0,\text{air}}\ [\Omega]$		$Z_{0,\text{SiO}_2}\ [\Omega]$
		Simulated	Calculated	Simulated
220	20	57	46.5	51
190	35	67.5	57.6	62.2
160	50	77.3	68.6	70.2
130	65	87.4	80.6	79.3
100	80	99	94.7	90
70	95	116	112.9	104

Table 4.1: 6 different CPW geometries with corresponding simulated characteristic impedances for aluminum coplanar waveguides with air and SiO_2 cladding and with the calculated analytically impedances for air cladding.

To be able to analyze losses, this set of 6 reference CPWs is designed in 4 lengths: 0.5 cm, 1 cm, 2 cm and 4 cm. In this way the general behavior of CPWs can be investigated, see Figure 4.5(a). Regarding the cell frame there are two regions that are covered with dielectric material of 0.5 cm each, and the rest remains surrounded by air, this is represented in Figure 4.2. Correspondingly the blue cuboid on Figure 4.5(b) is for the SiN layer and defines the

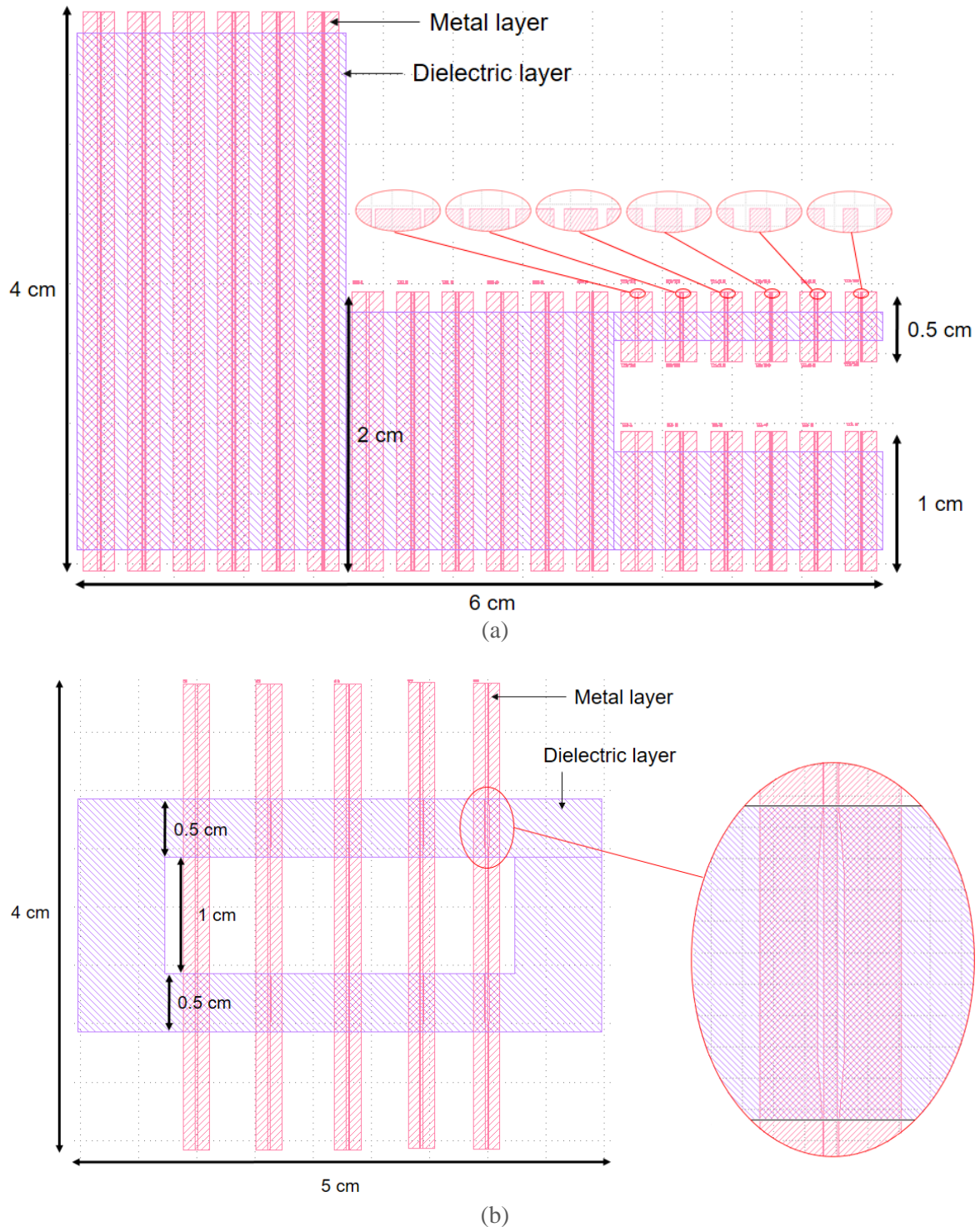


Figure 4.5: Mask layout designed in the mask drawing editor „K-Layout“: four sets of six coplanar waveguides with different geometries for different lengths to investigate the transmission lines characteristic generally (a) and coplanar waveguides designed for the vapor cell (b).

position of the glass frame for the subsequent bonding. Since the dielectric material enforces the capacitance as a function of relative permittivity, it therefore lowers the characteristic impedance as a function of capacitance, as given in section 2.1 by (2.22) and (2.21) respectively. To maintain the same impedance along the whole transmission line, the solution can be found by enlarging the space width in the regions under the frame. To achieve this several variations are applied to compare them after measurements: for example the strip width is fixed and the spacing width is increased stepwise, or, on the contrary, the spacing width is fixed and the strip width is increased stepwise. The resulting mask layout is depicted in Figure 4.5(b). Two layers are present on the layout: the layer at the bottom in pink represents metal and the blue one is of the dielectric material. The CPW's ground planes are chosen to be quite wide to make sure that no electric field is cut off. According to [6] even for even mode the ground plane width should be kept wide to avoid deviation of the characteristic impedance. Additionally, some narrow ground planes could also be included to the mask layout to see whether the ground plane width makes any difference for the characteristic impedance, as mentioned in [6]. The results of the simulation of the electric field is presented in Figure 4.6 and looks like described in Section 2.4 for the excited even mode of coplanar waveguide.

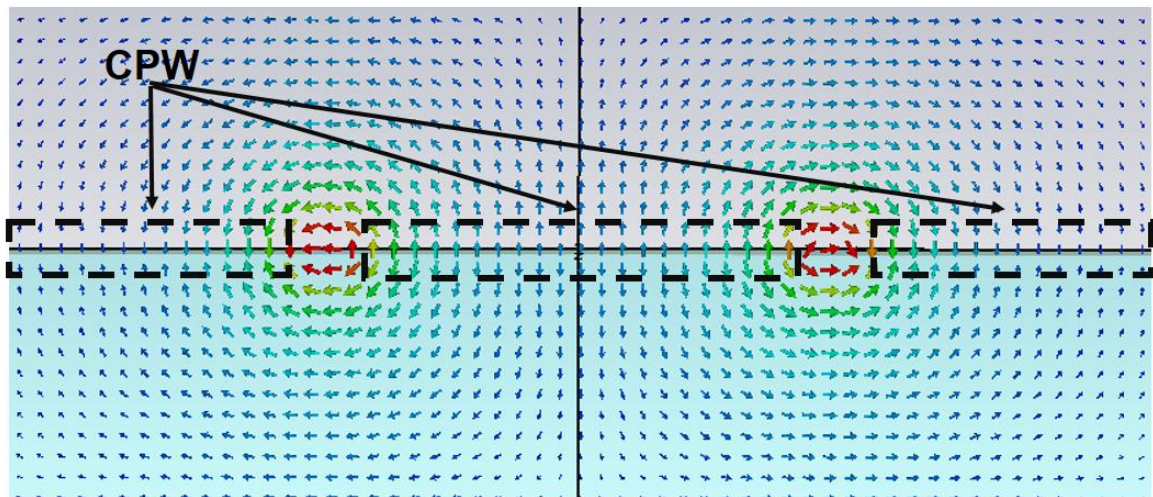


Figure 4.6: Simulated electric field distribution of the coplanar waveguide.

5 Fabrication

The fabrication process took place in the clean room of the Institute of Large Area Microelectronics' (IGM) with zones of classes 10 and 100.

With the purpose to test various materials, several wafers are fabricated using 1.1 mm XG¹ and borosilicate glass substrates with aluminum (Al), chromium (Cr) and a molybdenum-tantalum alloy (MoTa) as metallization layers and silicon nitride (SiN) as dielectric covering. All the substrates are first wet cleaned. After that they are covered with metals using a sputter deposition process [15]. This process starts with the creation of a plasma. Under an applied high voltage between the cathode ("target") and anode ("substrate") in the sputtering chamber, the electrons are released from the cathode surface and collide with the present gas atoms (usually argon), thus creating gas ions. These ions are then accelerated towards the target and bombard it with high energy, releasing the neutral target atoms. Ejected atoms travel through the plasma directly towards the substrate with low probability to be ionised, and are deposited on the substrate.

Next the wafers are prepared for structuring: they are covered with a positive photoresist and were exposed to UV light, using the same mask layout for all metals. The same process is applied for the silicon nitride layer structuring. After structuring the photoresist is developed in a chemical solution. While for metal etching two various techniques are applied, namely wet etching and reactive ion etching (RIE), the SiN layers are structured using RIE.

Several aluminum, one chromium and two molybdenum-tantalum CPWs are fabricated on the XG glass without a dielectric layer in order to compare the properties of these metals. In addition one wafer with MoTa metallization layer is wet etched and another one is dry etched using RIE [15]. While wet etching provides a high material selectivity due to properly selected chemicals, so that one layer can be fully etched without attacking the other film, the RIE etches everything under the ion beams, so that photoresist can be etched away and the underlying layer can be damaged. The disadvantage of the isotropic wet etching are the not perfectly perpendicular sides of the structures under the photoresist.

After fabrication the sheet resistance of both MoTa-CPWs was measured but no difference was found (see Table 5.1). One wafer with aluminum CPWs on XG glass substrate is covered with a silicon nitride (SiN) layer using plasma enhanced chemical vapor deposition (PECVD) [15]. In all other cases the dielectric is sputtered on the substrate. On the contrary to sputter deposition, which belongs to the category of physical vapor deposition (PVD), CVD forms the thin films from a gas state to a solid state due to chemical reactions. This process offers the advantage of higher film quality in terms of roughness and conformity, compared to the sputtering.

All the combinations of substrates, metals and dielectrics are presented in the Table 5.1.

¹ Alkaline earth boro-aluminosilicate glasses are specifically designed for high performance LCD's. The glass features high surface quality, excellent thermal properties, low density and high resistance to chemicals. Furthermore it contains no heavy chemicals and is thus considered environmentally friendly. [16]

	XG			Borosilicate		
	Me	t [nm]	R _s [Ω/□]	Me	t [nm]	R _s [Ω/□]
SiN (PECVD)	Al	118.5	0.33	-	-	-
SiN (sputter)				-	-	-
w/o SiN	Al	118.5	0.33	Al	116	0.33
	Cr	49.3	5.31			
	MoTa	50	3.44			
	MoTa (dry)	53.3	3.47			

Table 5.1: Metals chosen for fabrication on various glass substrates and (or without) dielectric material deposited using different techniques; (dry) is for RIE-etched MoTa layer, t is for thickness in [nm], R_s is sheet resistance in [Ω/□] taken with four point probe method.

The four point probe method is applied to measure the sheet resistance of metal films. The schematic measurement set is illustrated in Figure 5.1. That is, the current is driven through the pair of outer “current” pins; this causes the voltage drop in the region in between the outer pins. The pair of measuring “voltage” pins is connected to the impedance region to sense the voltage drop.

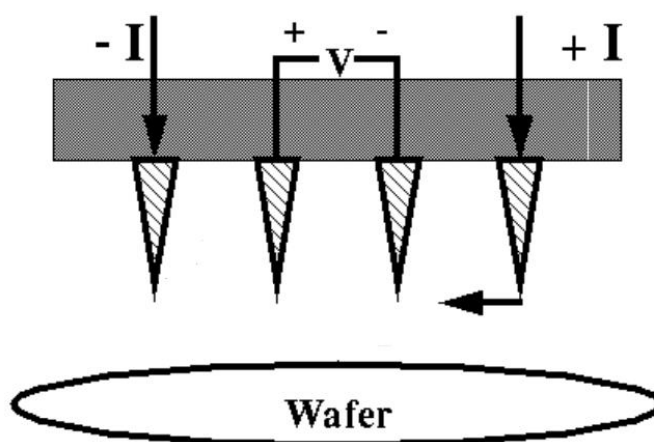


Figure 5.1: Schematic four point probe measurement set. Source: [17]

To compare the measured values with theoretical ones, the sheet resistances of the metals are calculated using the equation below:

$$R_s = \frac{\rho}{t} \left[\frac{\Omega}{\square} \right], \quad (4.1)$$

where ρ is the bulk resistivity in Ωm and t is the metal thickness in meters. The theoretical results as well as the measured values are listed in Table 5.2.

	Rho [Ωm]	Calculated R _s [Ω/□]	Measured R _s [Ω/□]	$\frac{\text{Measured } R_s}{\text{Calculated } R_s}$
Al	2.65×10^{-8}	0.228	0,33	~ 1.44
Cr	13×10^{-8}	2.64	5.31	~ 2
MoTa	8.8×10^{-8}	1.76	3.45	~ 2

Table 5.2: Specific resistivity, calculated and measured sheet resistance of aluminum, chromium and molybdenum-tantalum.

As can be seen, the measured sheet resistance of chromium and molybdenum-tantalum is approximately two times larger than calculated while the measured sheet resistance of aluminum deviates by a factor of 1.44 from the calculated value. Therefore it can be concluded, that aluminum layer is deposited more conform or that the nonconformity is less decisive for the slightly thicker layer.

After the CPWs are fabricated in the IGM's clean room, some substrates were bonded to the glass frame as described in section 3.2 in the laboratory of the 5th Institute of Physics.

6 Measurement results

The aim of the thesis is to design coplanar waveguides for a frequency of 100 MHz. Nevertheless the outlook for a wider frequency range is discussed in order to get a better understanding of the transmission line behavior and to have an outlook for future experiments at higher frequencies regarding various fabrication methods. The fabricated CPWs are measured in the laboratory of the Institute for Electrical and Optical Communications Engineering with a two-port vector network analyser. The measurement setup with the substrate and structured CPWs and with bonded glass frame on top of it is presented in Figure 6.1.

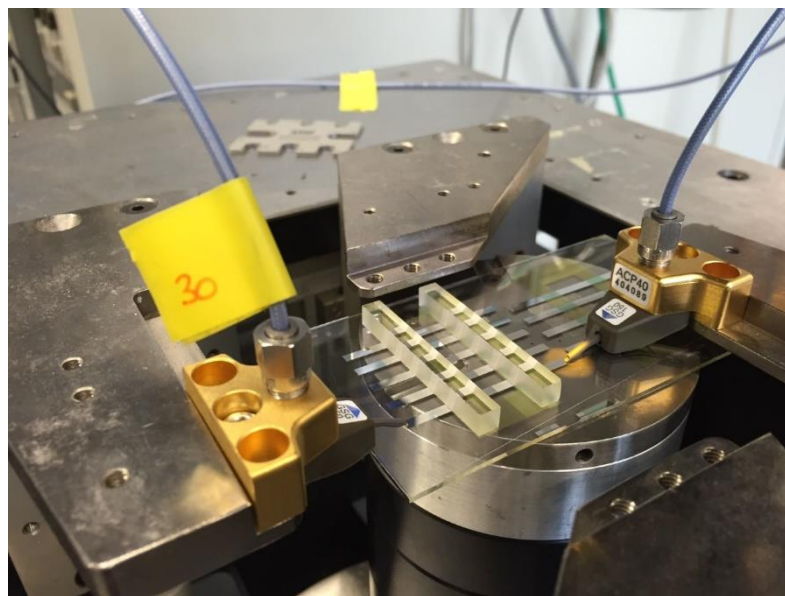


Figure 6.1: Set up of S-parameter measurement.

6.1 Overview over the measurement results

In this section the measuring results of the 4 cm long CPWs are discussed to compare various fabrication techniques considering higher frequencies for possible future experiments. Analysis of the CPWs is presented in the next sections.

Characteristics of various strip and space widths

In the first step the six reference CPWs mentioned in Chapter 4 are measured to find out, which geometry provides the best matching to the probes impedance. The parameters of three of six fabricated reference Al-CPWs of 4 cm length on borosilicate glass substrate are plotted in Figure 6.2. Only these three CPWs are chosen for the presentation of the overview; the curves of the other CPWs just lie in between.

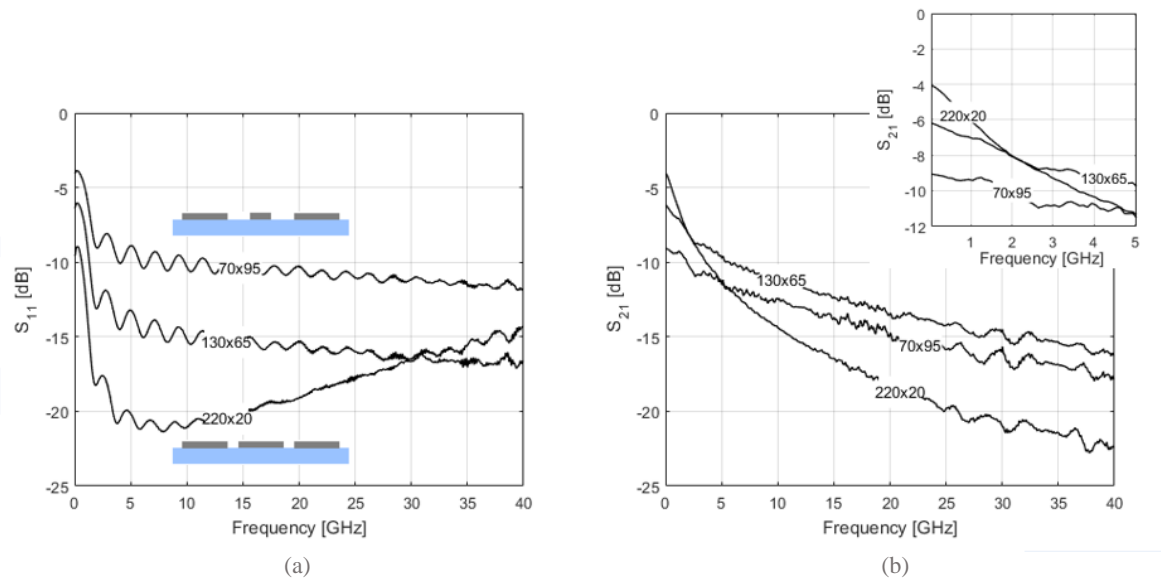


Figure 6.2: Reflection (a) and transmission (b) parameters of the 3 reference coplanar waveguides with the following strip and space width ($W_{\text{strip}} \times W_{\text{space}}$): $70 \mu\text{m} \times 95 \mu\text{m}$, $130 \mu\text{m} \times 65 \mu\text{m}$, $220 \mu\text{m} \times 20 \mu\text{m}$.

According to the simulations, the $220 \mu\text{m} \times 20 \mu\text{m}$ coplanar waveguide has the nearest to 50Ω impedance. It is exactly the case for 100 MHz considering the reflections, the curve lies lower under the curves of the others CPWs. Transmission of this CPW shows the best value at low frequencies, but from 5 GHz it changes its behavior to the worst transmission characteristic. The cause lies probably in the spacing width: the central strip and the ground plane are located close to each other, so that at growing frequencies more “leakage” current between the coplanar lines flows through the substrate. Further only straight CPWs with $220 \mu\text{m}$ strip width and $20 \mu\text{m}$ space width are discussed, if nothing else is pointed out, because they show better transmission at low frequencies which is the actual task of this thesis.

Comparison of different metals

In the second step the three metals: Al, Cr and MoTa are compared. They are all structured on XG glass. However, both XG and borosilicate glass showed just a very small difference in S-parameters and are not discussed further. The measurement results of the CPWs on borosilicate glass are presented in the Figure 6.3. The parameters of Al are much better, than the parameters of other metals. It shouldn't be forgotten, that the thickness of Al is approximately two times larger than the thickness of MoTa and Cr (see Table 5.1). Nevertheless, the ratio of Al to Cr or Al to MoTa thickness is still quite smaller than the ratio of their transmission parameters, which leads to the assumption, that the 50 nm Al layer still would have better characteristic than Cr or MoTa. It has to be noticed, that the Cr and MoTa are much harder: when contacting they are almost not scratched by the probes pins, in contrast to Al.

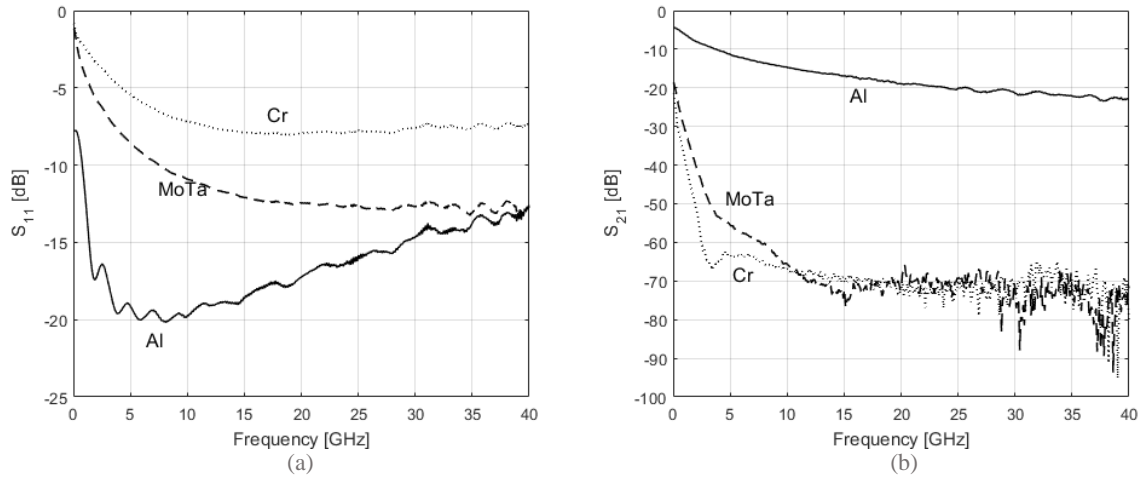


Figure 6.3: Reflection (a) and transmission (b) parameters of the Al, MoTa and Cr coplanar waveguides of 4 cm length.

Comparison of dry and wet etching

The wet etched and dry etched MoTa-CPWs are compared in Figure 6.4. The transmission of the dry etched CPWs at lower frequencies is clearly lower, it is approximately 20 dB below the transmission of the wet etched coplanar waveguide. The reason could be the damage from the ion beams, which can go through the photoresist and then through the thin metal layer. Another one assumption is that the ion beams attack the glass in the areas not covered with photoresist and etch it away, see the cross-sectional schematic view of the conducting strip of CPW after RIE. Probably the glass surface is also rough and the field lines could then be refracted and dissipated from the damaged glass surface. Generally, the fact that all the transmission curves are very scattered from the middle of the frequency range is probably due to skin depth, which shrinks with the frequency. A small reminder about the electric field lines arrangement along the coplanar waveguide, discussed in Section 2.4: They start on the center strip and land on the ground planes. With higher frequencies conducting area of a hot strip shrinks to the skin depth on the edges of the hot strip. Presuming because of it the transmission of the wet etched CPW becomes lower than the transmission of plasma etched CPW at higher frequencies. The edges can be undercut during etching process by the

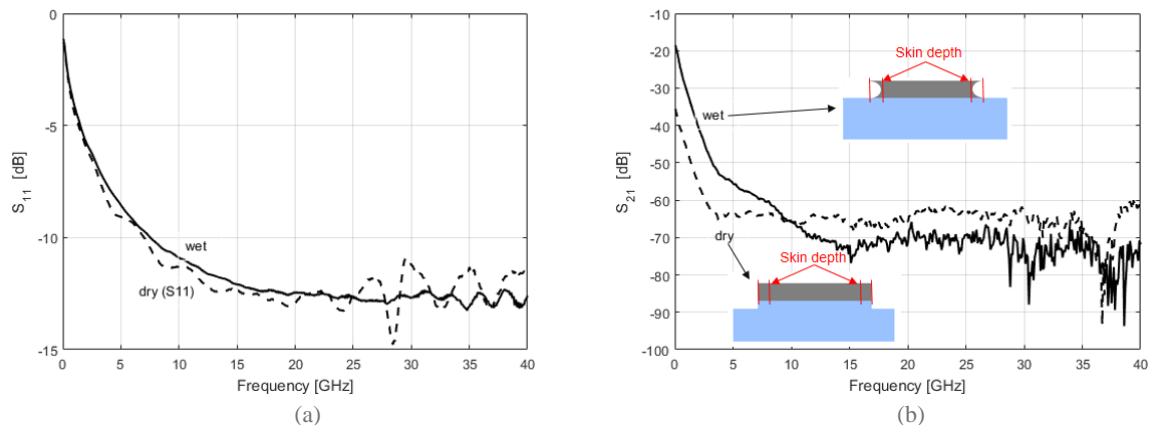


Figure 6.4: Reflection (a) and transmission (b) parameters of the 4 cm MoTa coplanar waveguides wet etched and dry etched.

chemical solution and there is less metal left for small skin depths. It means more losses and more sensitivity to film quality with decreasing conducting area. The skin depth varies from $14.7 \mu\text{m}$ at 45 MHz to $0.49 \mu\text{m}$ at 40 GHz according to Equation (2.35), which is still larger as the CPW's thickness. In Figure 6.4(a) both reflection parameters are plotted.

The CPWs were measured at the same day one after another, so that the calibration or others disturbances couldn't influence the measurement results.

Comparison of physical and chemical vapor deposition

The type of the dielectric material deposition (PVD or CVD) of a 200 nm thick layer doesn't influence the CPW transmission characteristic at low frequency. This can be seen in Figure 6.5. At higher frequencies it makes some difference: The reflection of the CPW with sputtered SiN is much more scattered, which leads to conclusion that its quality is lower than that of chemically deposited. But still the reflection parameter is better than that of chemically deposited CPW. The transmission characteristic at higher frequencies is slightly better for the chemically deposited SiN layer.

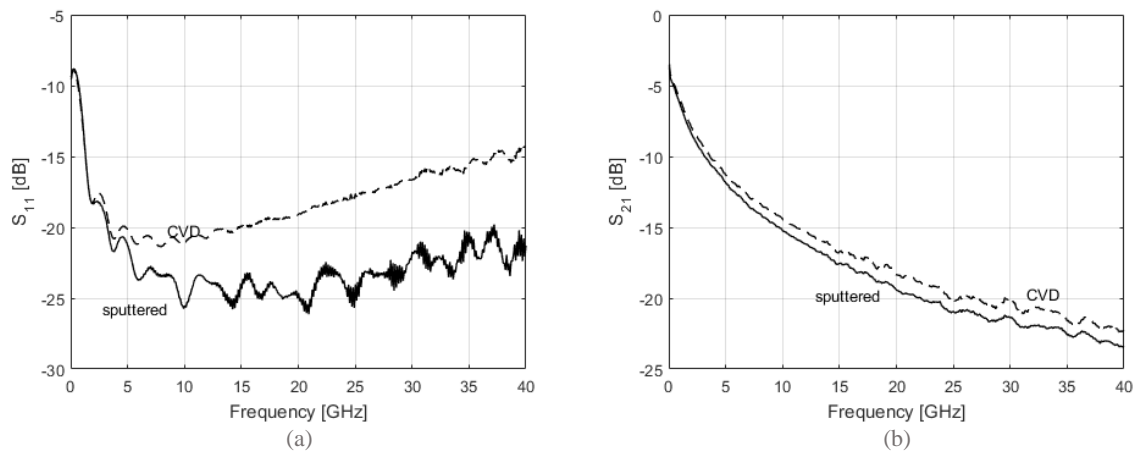


Figure 6.5: Reflection (a) and transmission (b) parameters of the 4 cm Al coplanar waveguides with 200 nm SiN sputtered and CV deposited.

Considering the target cell structure, where there are two sections of 0.5 cm each, which are covered with SiN, also the measurements of short CPWs are done (while all previous measurements were done for the 4 cm long CPWs). They are presented in Figure 6.6. The CPW with the chemically deposited SiN is much more sensitive to the wave length, compared to the sputtered version due to the high-quality of the deposited material; there are two clearly defined resonance places. As to the transmission, the curve probably shows the attenuation mechanism due to the dielectric loss described in Section 2.2.2. Since the dielectric loss is proportional to the frequency and the ohmic losses are proportional to the square root of frequency, according to Equations (2.58) and (2.37) respectively, at some point the dielectric losses would dominate the ohmic losses. The sputtered SiN could be less conform and therefore not much energy is needed to damp the vibrating dielectric dipoles comparing to the high quality CV deposited layer. Interestingly the transmission of the CPW with CVD-SiN is better for 4 cm long CPW and worse for the 0.5 cm CPW, comparing to PVD. Seemingly for the larger length there are more losses due to the film quality of the sputtered material, so that they became more significant than dielectric losses of consistent CVD layer. Eventually the sputtered CPW show better performance for both reflection and transmission parameters.

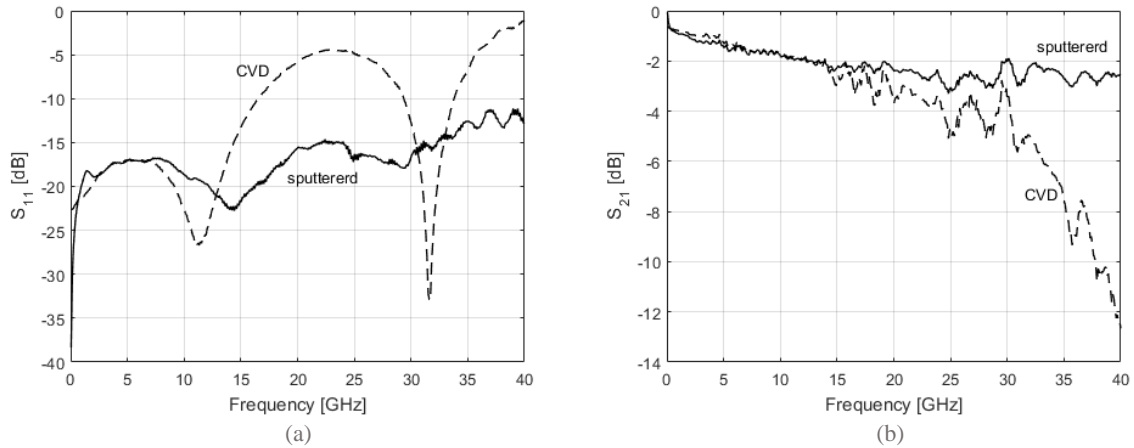


Figure 6.6: Reflection (a) and transmission (b) parameters of the 0.5 cm Al coplanar waveguides with 200 nm SiN sputtered and CV deposited.

As already mentioned in Chapter 4, some CPWs were designed to be put under the glass frame (see Figure 4.5). These CPWs are partly covered with SiN layer and along these covered sections the space width are enlarged to maintain the characteristic impedance same along the transmission line length. Their S-parameter curves don't differ much, thus just the straight CPWs without any discontinuities under the frame region are considered further.

6.2 Analysis of simulations and measurements

In this section the simulated and measured results of 0.5 cm long CPWs are compared and discussed.

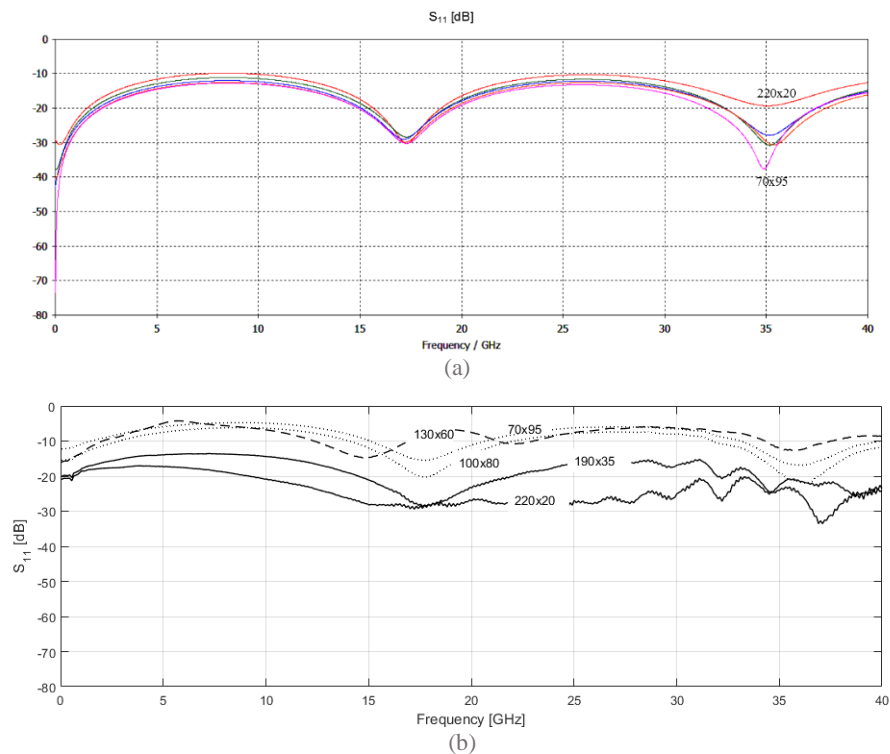


Figure 6.7: Reflection parameters of (a) simulated and (b) measured coplanar waveguides.

Consider the CPW with air cladding. The S_{11} parameters of the six reference CPWs are presented in the Figure 6.7. There are two resonance points on the plot with simulated curves, those are the notches at a frequency of approximately 17.5 GHz and 35 GHz. If calculating the wavelengths in medium for these frequencies the values of approximately 1 cm and 0.5 cm respectively are obtained. Therefore at a frequency of 17.5 GHz the CPW length corresponds to the half of the wavelength and at a frequency of 35 GHz the CPW length corresponds to the one wavelength. As to the measured reflexion parameters, the notches of some CPWs are slightly shifted towards a higher frequency. It can be explained by the relative permittivity. For the simulations the relative permittivity of 4.6 for borosilicate glass is taken. Actually it can vary from approximately 3.9 to 4.6 and after resimulation of CPW with the permittivity of borosilicate glass of 4.0 the notches almost coincide. In Figure 6.8 the simulations with the initially used relative permittivity of 4.6 and adjusted permittivity of 4.0 in terms of propagation constant are presented for the CPW with the strip width and space width $220 \mu\text{m} \times 20 \mu\text{m}$. Further only this CPW is discussed as it showed the best reflection and transmission characteristic for the target frequency of 100 MHz in the previous section.

The propagation constant of the measured parameter is extracted from the wave equation along the propagation direction z :

$$E(z) = Ee^{-\gamma z}, \quad (6.1)$$

then solving the equation for γ and taking its imaginary part. In this way the simulated and the fabricated CPWs are in good agreement.

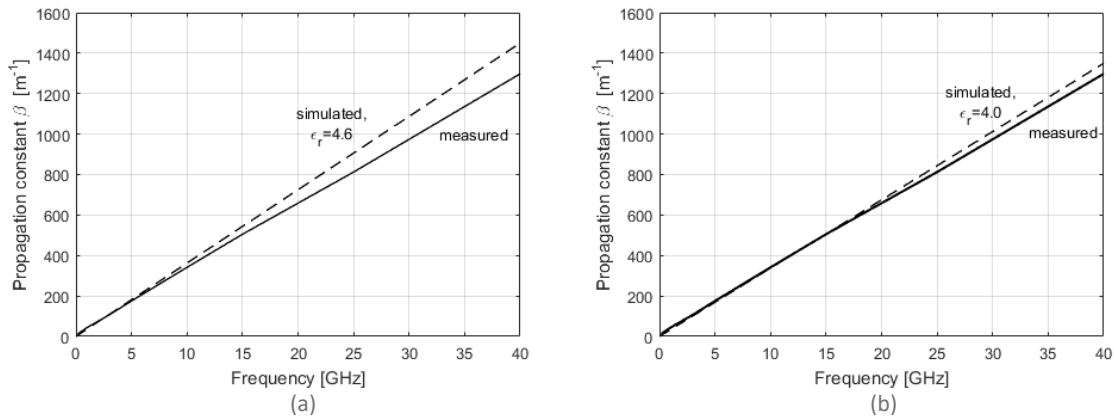


Figure 6.8: Measured propagation constant compared to the simulated propagation constant with relative permittivity of the borosilicate glass $\epsilon_r = 4.6$ (a) and $\epsilon_r = 4.0$ (b).

At this point all four scattering parameters for 0.5 cm CPW are presented. In Figure 6.9 all the simulated parameters are plotted and in Figure 6.10 all the measured parameters. The reflection parameters as well as the transmission parameters of the simulated CPWs are perfectly symmetrical. Essentially the same can be stated for the fabricated CPWs.

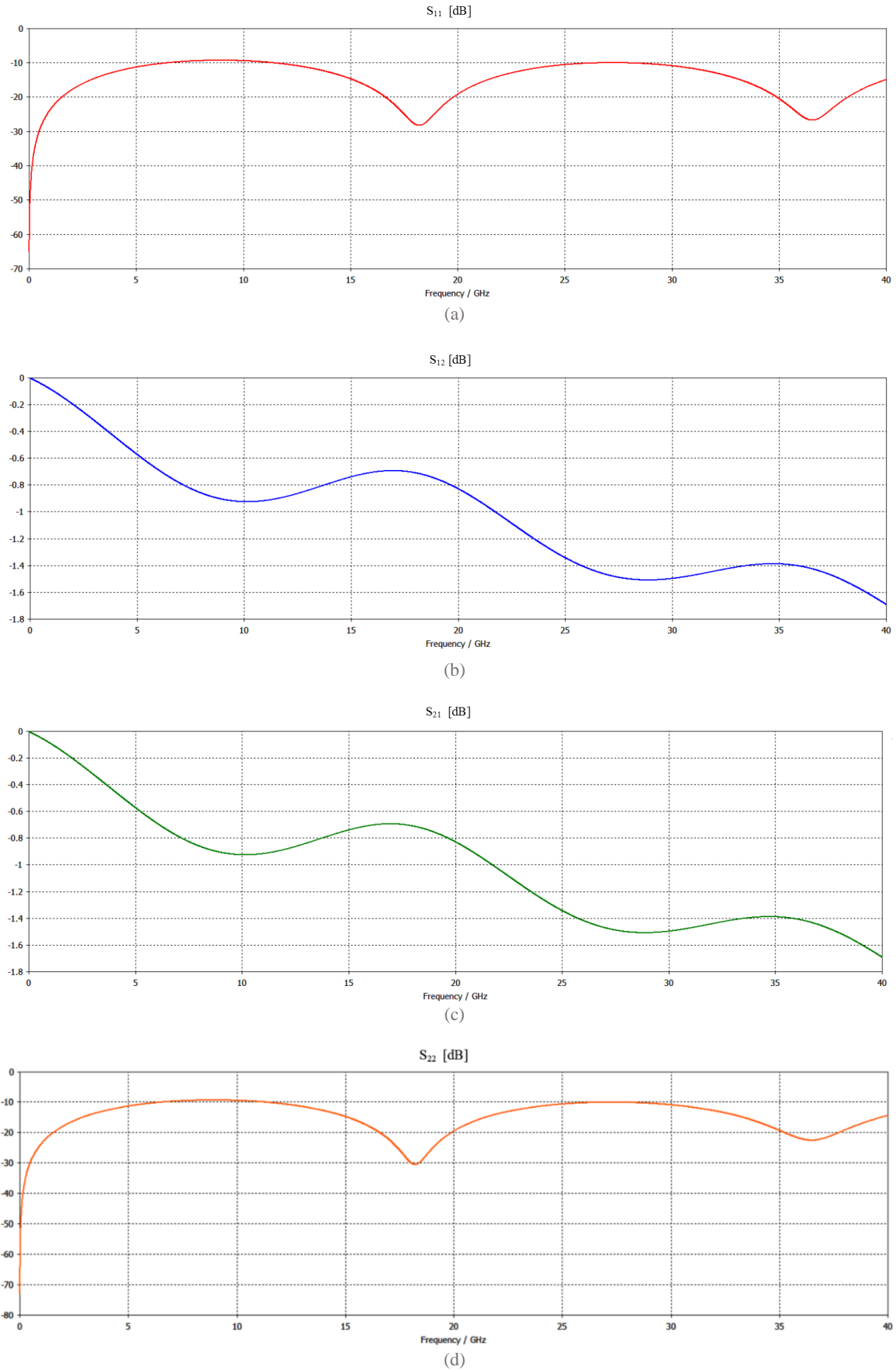


Figure 6.9: Simulated (CST[®] MWS[®]) scattering parameters of the 0.5 cm aluminum coplanar waveguide with air cladding: S_{11} (a), S_{12} (b), S_{21} (c) and S_{22} (d), represented in dB; $W_{\text{strip}} = 220 \mu\text{m}$, $W_{\text{space}} = 20 \mu\text{m}$.

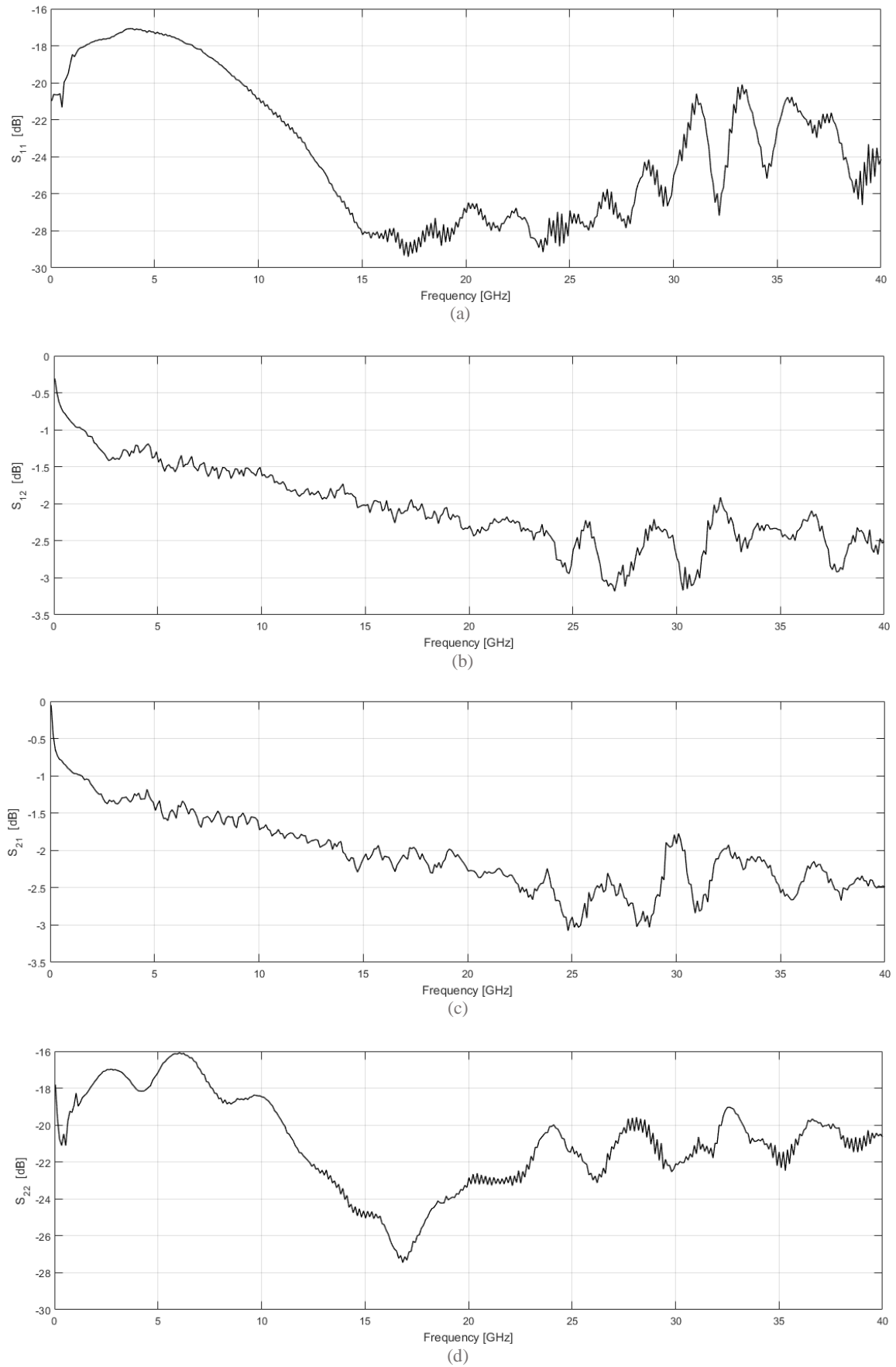


Figure 6.10: Measured scattering parameters of the 0.5 cm aluminum coplanar waveguide with air cladding: S_{11} (a), S_{12} (b), S_{21} (c) and S_{22} (d), represented in dB; $W_{\text{strip}} = 220 \mu\text{m}$, $W_{\text{space}} = 20 \mu\text{m}$.

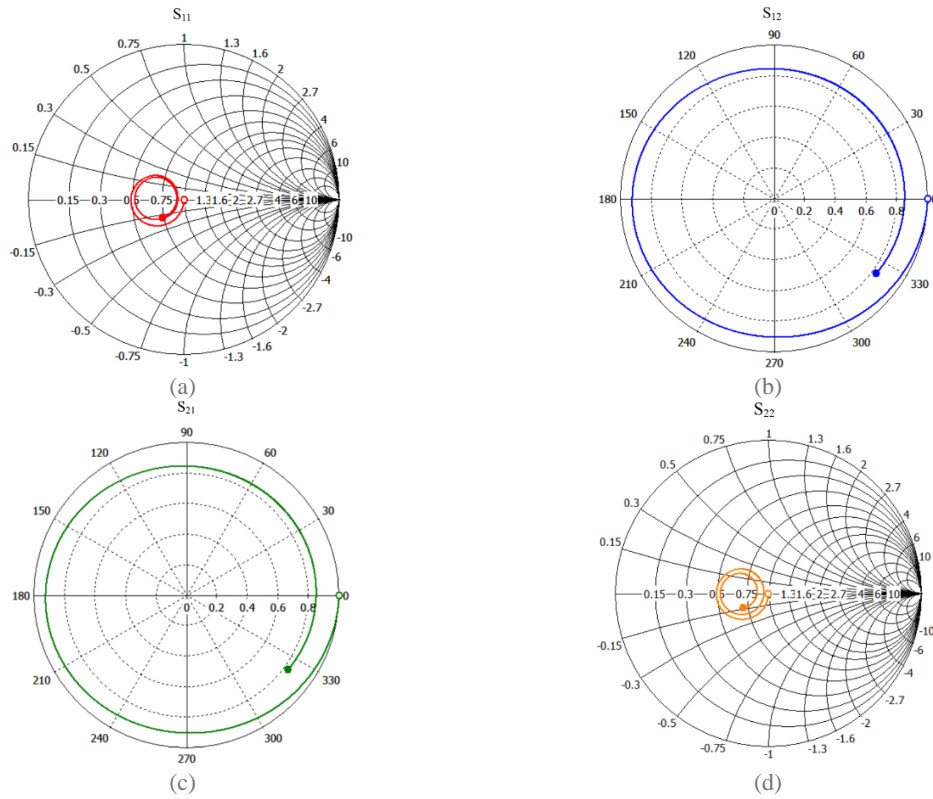


Figure 6.11: Simulated (CST[®] MWS[®]) scattering parameters of the 0.5 cm aluminum coplanar waveguide with air cladding: S_{11} (a), S_{12} (b), S_{21} (c) and S_{22} (d), represented in Smith chart; $W_{\text{strip}} = 220 \mu\text{m}$, $W_{\text{space}} = 20 \mu\text{m}$.

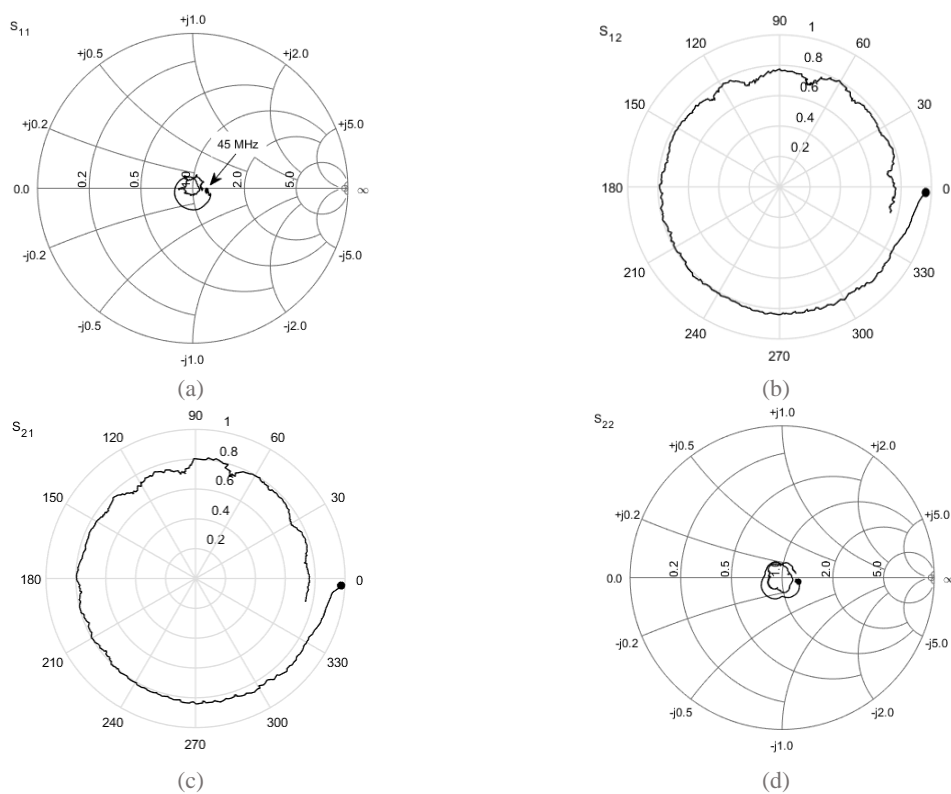


Figure 6.12: Measured after fabrication scattering parameters of the 0.5 cm aluminum coplanar waveguide with air cladding: S_{11} (a), S_{12} (b), S_{21} (c) and S_{22} (d), represented in Smith chart; $W_{\text{strip}} = 220 \mu\text{m}$, $W_{\text{space}} = 20 \mu\text{m}$.

In Figure 6.11 and in Figure 6.12 the reflection parameters in Smith chart and transmission parameters in polar graph of simulated and measured CPWs respectively are represented. From both Smith chart and polar graph is seen, that the phase trip is shorted for the fabricated waveguides. This is because wavelength is larger for the fabricated CPWs due to the smaller reduction factor (square root of effective relative permittivity of ~ 4.0) compared to the wavelength of simulated CPWs (square root of 4.6). Also the smaller magnitude of both reflection and transmission curves can be noticed.

In Figure 6.13 the S-parameters of the CPWs with different lengths are presented. The lengths are each time doubled; the losses are approximately doubled as well accordingly to the lengths. As already discussed in the first section, there are two dominating loss mechanism. While speaking about air cladding, the loss tangent is negligibly small, thus the dielectric losses can be ignored. In this way the major attenuation sources are ohmic losses and radiation.

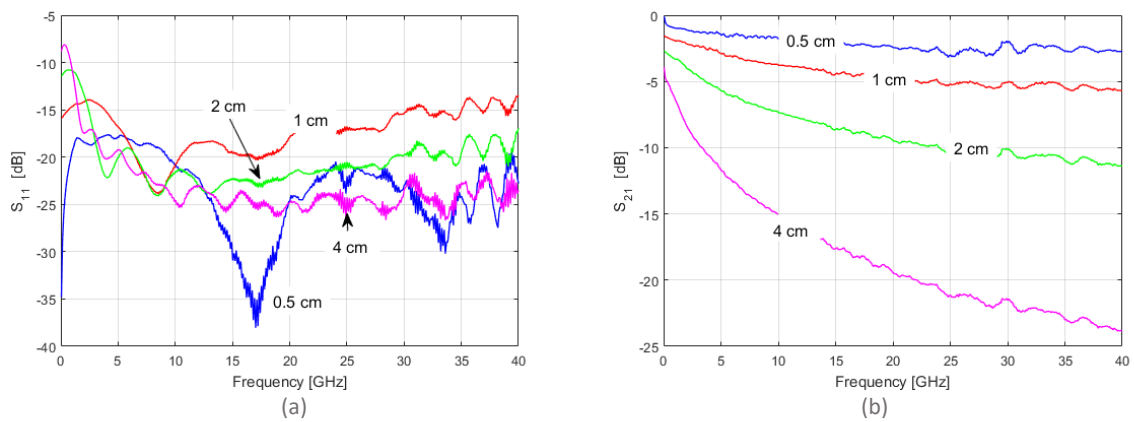


Figure 6.13: Reflection (a) and transmission (b) parameters of coplanar waveguides with different lengths.

For longer CPWs the reflection is high at low frequencies and much lower at high frequencies. The always declines. Probably at increasing frequencies there is a lot of radiation, so that CPWs emit part of the power before it reaches the load. The CPWs act therefore as infinite transmission line where no reflection occurs [1].

The input impedance of the transmission line can be calculated rearranging Equation (2.60):

$$Z_{in} = Z_{load} \frac{1-r}{1+r}. \quad (5.3)$$

Thus, the calculated input impedance of the fabricated transmission line is plotted in Figure 6.14 along with the calculated analytically impedance and the real part of the simulated impedance. While the analytical solution is frequency and material independent, the simulated and “measured” ones change with phase. Generally the impedance wave of the fabricated CPWs is a bit larger than was simulated. The reason can be the smaller self-inductance of the CPWs due to the metal layer imperfection and therefore deviating from simulation value. Interestingly that, the measured impedance is nearer to the calculated impedance than to the simulated at 100 MHz.

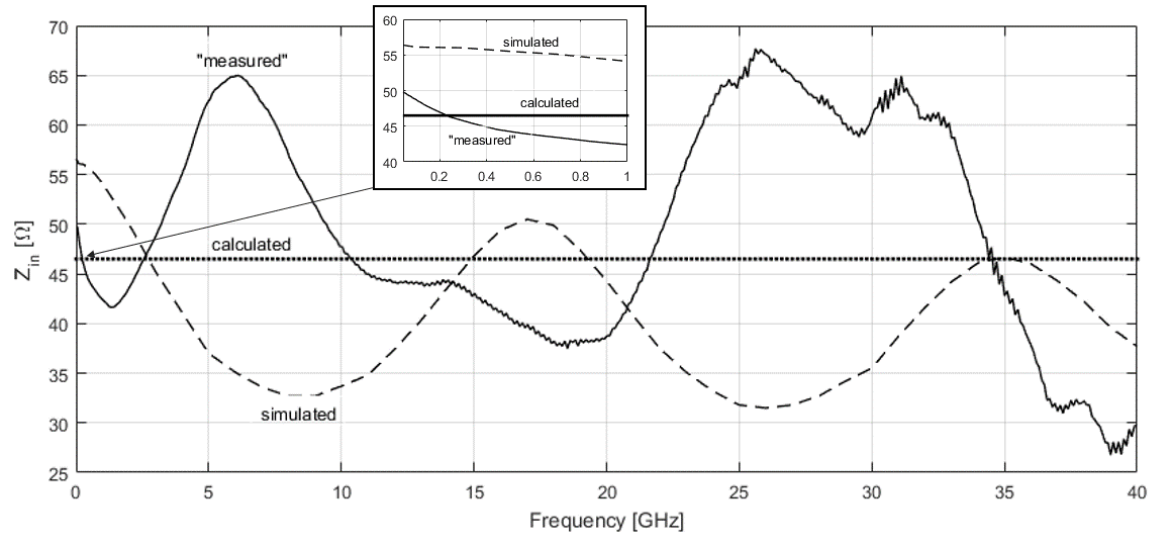


Figure 6.14: Analytically calculated, simulated and calculated from measurements input impedance of the 0.5 cm coplanar waveguide.

6.3 Final structure of the coplanar waveguide

Finally target CPW for integration into the vapor cell is discussed. Figure 6.15 presents the reflection and transmission characteristic of straight 4 cm long Al-CPW after bonding, i.e. with SiO_2 cladding over two 0.5 cm long sections along the line.

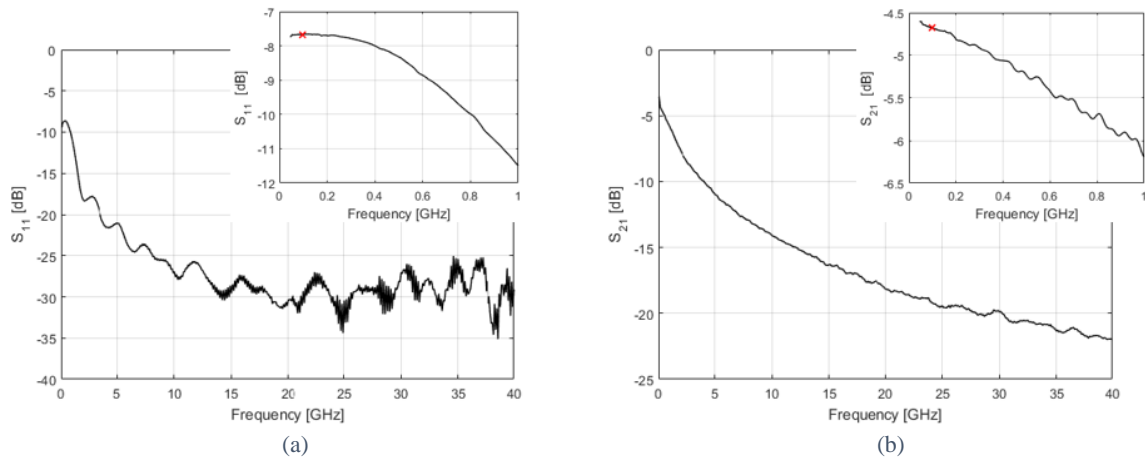


Figure 6.15: Reflection (a) and transmission (b) characteristic of the 4 cm long Al coplanar waveguides without discontinuities and with bonded frame with $W_{\text{strip}}=220 \mu\text{m}$ and $W_{\text{space}}=20 \mu\text{m}$.

At a frequency of 100 MHz losses of approximately 4.6 dB are obtained. Before bonding the losses for this frequency were around 0.5 dB higher. As the dielectric contributes quite noticeable losses, the enhancement is due to temperature annealing, which took place during frame bonding, when the wafer was heated to 300°C.

7 Summary and outlook

During this work transmission lines for experiments with Rubidium vapor cell at a frequency of 100 MHz are designed and fabricated. A coplanar waveguide is thereby the most suitable solution regarding fabrication, because less steps are required as for a microstrip line. Moreover coplanar waveguide has two degrees of freedom comparing to a microstrip line, strip width and space width, to manipulate the characteristic impedance and doesn't support radiation in the substrate like backed transmission lines do. Because of the unusual transmission line parameters as length in cm scale and thickness in nm scale several design variations are drafted, namely coplanar waveguides with various strip and space widths, which provides approximately 50Ω to 100Ω characteristic impedance. Hence, even if some inaccuracies in a simulation or some deviations due to fabrication occur, there are still several structures among which the appropriate coplanar waveguide can be found. Eventually the simulation and fabrication show quite accurate performance. Another one variation refers to the coplanar waveguide length. Coplanar waveguides were structured in four lengths each time doubled, from 0.5 to 4 cm. This provides a convenient way to investigate how the attenuation changes. The measurement show that the attenuation increases proportionally to the length variation, so that if length doubles, the attenuation is also approximately two times higher. All these steps were taken in order to examine the general behavior of the coplanar waveguides. As to the target structure, there are two sections that are covered with silicone dioxide where glass substrate is bonded to the frame. The dielectric lowers the characteristic impedance and in attempt to maintain the same impedance along the whole length the spacing distance is increased. However just a slight improvement is achieved so that straight coplanar waveguide without discontinuities is selected. The coplanar waveguide is measured before and after the bonding process of the glass substrate to the cell frame. The resulting losses after bonding yield approximately 4.6 dB for the coplanar waveguide of 4 cm length and 115 nm thickness at frequency of 100 MHz, which is approximately 0.5 dB higher than before bonding. As silicone dioxide formed during bonding above the coplanar waveguides brings in additional dielectric losses, the enhancement is due to temperature annealing during bonding. Casually during fabrication several structuring methods and materials are applied and compared in order to have an outlook for potential future experiments at higher frequencies. For example aluminum shows the better performance compared to the molybdenum tantalum and chromium due to its higher conductivity and property to form immediately the oxide layer, which protect the metal layer during fabrication. Also the etching technique can influence the film characteristic drastically. In the course of this work the fabricated coplanar waveguides are carefully compared with the simulations and are found to be in good agreement, excepting losses. Due to the measurement of a sheet resistance of the coplanar waveguides after structuring, the actual specific resistivity is calculated and compared with the theoretical specific resistivity, which is used in literature and in the simulation software. It gives the degree of imperfection of the structured metallic layer. As it is the only parameter that changes from the simulation to the fabrication, the losses have to be proportional to the resistivity increase. But it is seen that losses are higher, which means that more energy is radiated. This bachelor thesis is the first attempt to design a suitable transmission lines for the experiments with atomic vapor cell. Therefore more research should be done to realise a better performance and higher bandwidth of the coplanar waveguides. But the main improvement can be achieved by reduction of the cell size, which automatically makes the coplanar waveguides shorter and minimizes the losses significantly.

Appendix

Simulation in CST® MWS®

By starting CST STUDIO SUITE new project is created using “Circuits & Components” template of MW & RF & Optical application area, see Figure 7.1.

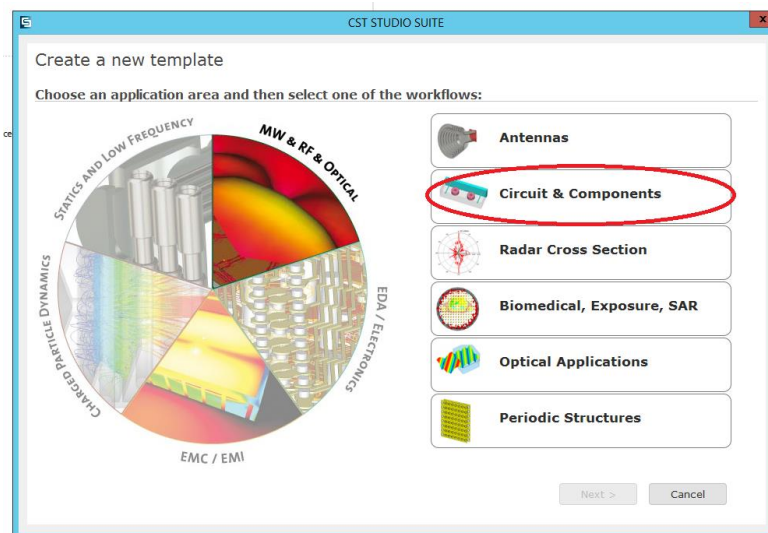


Figure 7.1: Pop-up menu for creation of a new project.

After clicking on “Circuits & Components” button the “Waveguide & cavity Filters” workflow can be chosen. The units can be defined in the next step in the proposed menu or it can be proceeded with the default values, which can be changed during work session. The same applies for frequency and solver in the next two steps. For the simulation of the coplanar waveguides a solver in frequency domain is applied.

When the project is created, the structure can be constructed using different shapes in menu “Modelling”. By clicking on the needed shape and pressing “esc” the window pops up, where the shape geometries and location can be defined. The materials are chosen in this step by loading them from the material library or by creating a new material, see Figure 7.2. For convenience parameters can be defined and saved in the parameter list window before modelling. Boolean operations can be applied to shapes in order to unite them, subtract, intersect etc.

In menu “Home” units and setup solver can be redefined. After each geometrical change the parameters should be updated by the command “Parametric Update”.

In the menu “Simulation”, frequency, background and boundaries have to be set up, the commands on the very left of the menu panel. Background is set on “Normal” in all directions. The boundaries are set on “open” in all directions. Additionally symmetry planes can be defined to decrease the computation work. Field monitor can be set in this menu. Such functions as “Parametric Sweep” and “Optimizer” can facilitate the simulation.

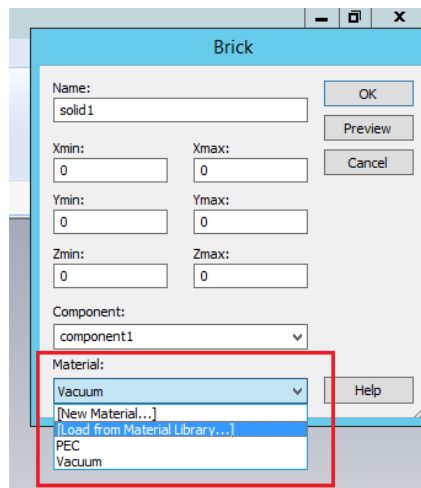


Figure 7.2: Pop-up menu for shape creation.

“Waveguide Port” feeds the power and has 50Ω impedance. For analysing of all four scattering parameters, waveguide ports on the input and on the output of the transmission lines have to be created. The waveguide port represents an infinitely long hollow waveguide and therefore suitable port geometries have to be set up. In case of an ungrounded coplanar waveguide, the height of the port has to be not less than the sum of the middle strip width and two space widths; the width of the port should be approximately two-three times larger than port height.

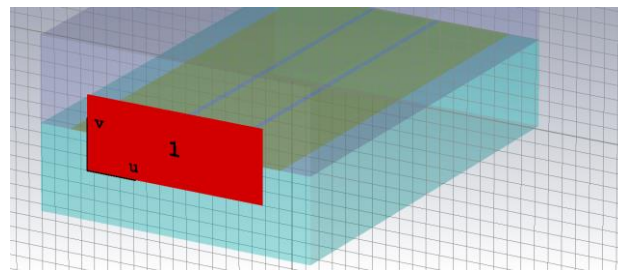


Figure 7.3: Simulation view of the waveguide port of the coplanar waveguide.

Starting the solver with button “Setup Solver”, “General purpose” method can be chosen with the “Tetrahedral (legacy)” mesh type. Also it is necessary to check on the “Adaptive tetrahedral mesh refinement” button. This automatically adjusts the mesh quality till the deviations between the adjustment steps are negligible. In this step “Acceleration” should be set up at maximum 5 threads for “Multithreading (CPU)”. This simulation parameters are shown in Figure 7.4.

The mesh can be viewed during and after the simulation process by clicking on “Mesh View” in the menu “Simulation”. The results are to be found in the navigation tree on the left in the folders “1D Results”, “2D/3D Results” etc. The S-Parameters can be represented in different plot types proposed in menu “1D Plot” in the upper menu panel after choosing one of parameters. For example, the S_{11} parameter can be plotted in Smith Chart and the characteristic impedance of the transmission line is given in the top left corner. Port information and field patterns are saved in the folder “2D/3D results”.

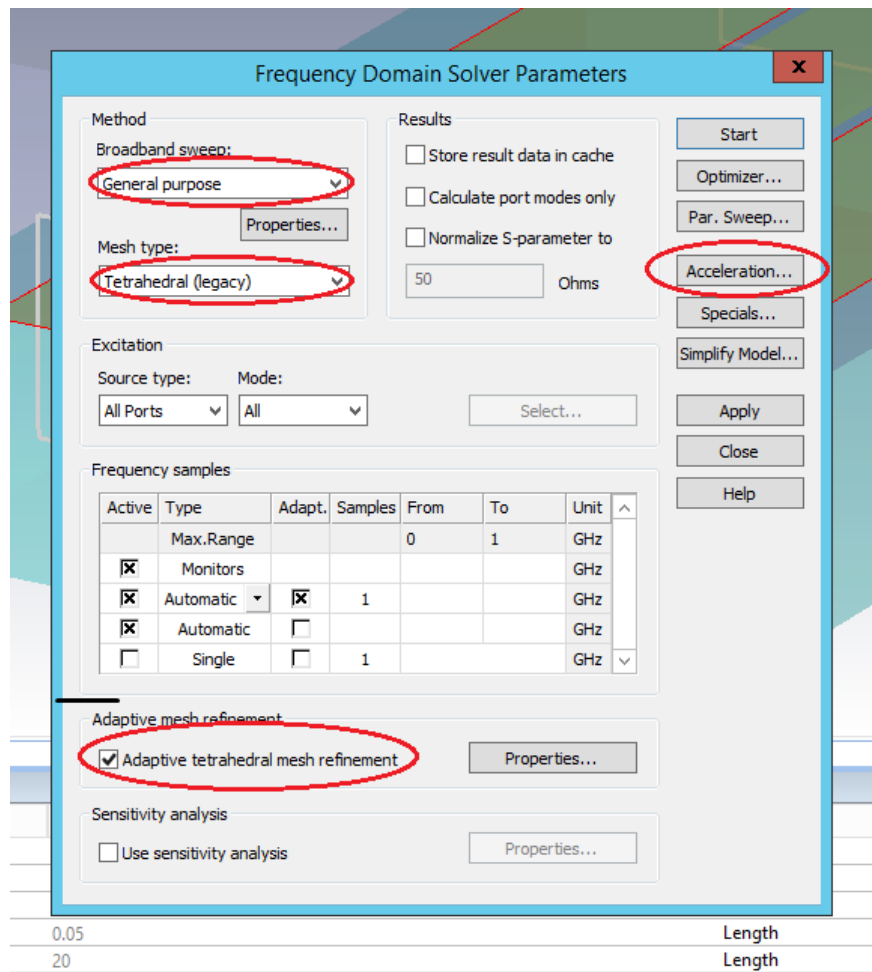


Figure 7.4: Frequency domain simulation parameters used for the simulation of the coplanar waveguides.

Bibliography

- [1] David M. Pozar
Microwave Engineering, 4th ed.
John Wiley & Sons, Inc., 2011
- [2] Kai Chang
Handbook of RF/Microwave Components and Engineering
John Wiley & Sons, Inc., Hoboken, New Jersey, 2003
- [3] Donald G. Fink, H. Wayne Beaty
Standard Handbook for Electrical Engineers, 14th ed.
McGraw-Hill, London, 2000
- [4] Nathan Ida
Engineering Electromagnetics, 3rd ed.
Springer. Available: <http://link.springer.com/book/10.1007%2F978-3-319-07806-9>
- [5] M. Kummer
Grundlagen der Mikrowellentechnik
VEB Verlag Technik, Berlin, 1986
- [6] Ingo Wolf
Coplanar Microwave Integrated Circuits
John Wiley & Sons, Inc., Hoboken, New Jersey, 2006
- [7] Brian C. Wadell
Transmission line design handbook
Artech House, 1991
- [8] M. Abramowitz, I.A. Stegun
Handbook of mathematical functions with: Formulas, Graphs and Mathematical Tables
U.S. Government Printing Office, 1972
- [9] R. Daschner
Addressable Rubidium vapor cells for optical and electrical read-out of Rydberg excitations
5th Institute of Physics of the Stuttgart University, 2015
Available: http://www.pi5.unistuttgart.de/common/show_file.php/finished_thesis/147/beschaenkt/thesis.pdf
- [10] H. Fan, S. Kumar, J. Sedlacek, H. Kübler, S. Karimkashi and J. P. Shaffer
Atom based RF electric field sensing
J. Phys. B: At. Mol. Opt. Phys. 48 (2015) 202001 (16pp)
- [11] A. Gaetan, Y. Miroshnychenko, T. Wilk, A. Chotio, M. Viteau, D. Comparat, P. Pillet, A. Browaeys, and P. Grangier
Observation of collective excitation of two individual atoms in the Rydberg blockade regime.
Nature Physics, 5:115–118, 2009. Available: <https://arxiv.org/abs/0810.2960>

-
- [12] L. Isenhower, E. Urban, X.L. Zhang, A.T. Gill, T.A. Johnson, T.G. Walker, and M. Saffman
Demonstration of a Neutral Atom Controlled NOT Quantum Gate.
Phys. Rev. Lett., 104:010503, 2010.
Available: <https://journals.aps.org/search/results?sort=relevance&clauses=%5B%7B%22operator%22:%22AND%22,%22field%22:%22title%22,%22value%22:%22Demonstration%20of%20a%20Neutral%20Atom%20ControlledNOT%20Quantum%20Gate%22%7D%5D>
- [13] A. Berthold, L. Nicola, P.M. Sarro, M.J. Vellekoop
Glass-to-glass anodic bonding with standard IC technology thin films as intermediate layers.
Sensors and Actuators 82 (2000) 224-228
- [14] R. Daschner, H. Kübler, R. Löw, H. Bauer, N. Frühauf, and T. Pfau
Triple stack glass-to-glass anodic bonding for optogalvanic spectroscopy cells with electrical feedthroughs.
Appl. Phys. Lett., 105:041107, 2014
- [15] C.Y. Chang and S.M. Sze
ULSI Technology
McGraw-Hill, 1996
- [16] <http://abrisatechnologies.com/wp-content/uploads/2014/03/Corning-Eagle-XG.pdf>
- [17] http://www.cen.iitb.ac.in/slotbooking/RECEPIES/140_RECEPIES.pdf

Acknowledgement

I am cordially thankful to all who helped me during my bachelor thesis. At first place to my supervisors, María Félix Rosa from the Institute for Electrical and Optical Communications Engineering and Johannes Schmidt from 5th Institute of Physics and Institute of Large Area Microelectronic at University of Stuttgart, for their enthusiasm and a lot of support.

I would like to thank to Dr.-Ing. Wolfgang Vogel from the Institute for Electrical and Optical Communications Engineering and to Dr. Harald Kübler from 5th Institute of Physics at University of Stuttgart for their friendly manner and useful advices and remarks.

Also I would like to thank to Utpal Dey from Institute of Radio Frequency Technology at University of Stuttgart who always helped me whenever I asked for it.

Finally, I would like to express my profound gratitude to my family, my uncle Felix Liber and my aunt Katerina Liber, and to my cousins Leonid and Valentina Liber who gave me the opportunity to study in Germany and who support me with love and dedication through my way.

Thank you a lot.

Erklärung

Ich versichere hiermit, dass ich die vorliegende Diplomarbeit selbstständig verfasst und keine weiteren als die angegebenen Hilfsmittel benutzt habe. Die Stellen der Arbeit, die anderen Werken dem Wortlaut oder dem Sinn nach entnommen sind, wurden durch Angabe der Quellen sichtbar gemacht.

Diese Arbeit hat in gleicher oder ähnlicher Form noch keiner anderen Prüfungsbehörde vorgelegen und wurde auch noch nicht in gleicher oder ähnlicher Form an anderer Stelle veröffentlicht.

Das elektronische Exemplar stimmt mit der Papierform überein.

I declare that this thesis is my original work and that only the indicated means have been used in this draft. Parts that are quotes or paraphrases of other works are identified as such by indicating the references.

This thesis has not been submitted in any form for another degree or diploma at any university or other institution and has not been published elsewhere.

The electronic version is identical to the printout.

Stuttgart, den 22.11.2016

Nachname: Guguieva Vorname: Kateryna

Unterschrift: _____